

HIGH RESOLUTION SEARCH FOR DARK MATTER AXIONS IN MILKY
WAY HALO SUBSTRUCTURE

By

LEANNE DELMA DUFFY

A DISSERTATION PRESENTED TO THE GRADUATE SCHOOL
OF THE UNIVERSITY OF FLORIDA IN PARTIAL FULFILLMENT
OF THE REQUIREMENTS FOR THE DEGREE OF
DOCTOR OF PHILOSOPHY

UNIVERSITY OF FLORIDA

2006

ACKNOWLEDGMENTS

This work is based on research performed by the Axion Dark Matter eXperiment (ADMX). I am grateful to my ADMX collaborators for their efforts, particularly in running the experiment and providing the high resolution data. Without these efforts, this work would not have been possible.

I thank my advisor, Pierre Sikivie, for his support and guidance throughout graduate school. It has been a privilege to collaborate with him on this and other projects. I also thank Dave Tanner for his assistance and advice on this work.

I would like to thank the other members of my advisory committee, Jim Fry, Guenakh Mitselmakher, Pierre Ramond, Richard Woodard and Fred Hamann, for their roles in my progress. I am also grateful to the other members of the University of Florida Physics Department who have contributed to my graduate school experience.

I am especially grateful to my family and friends, both near and far, who have supported me through this long endeavor. Special thanks go to Lisa Everett and Ethan Siegel.

TABLE OF CONTENTS

	<u>page</u>
ACKNOWLEDGMENTS	ii
LIST OF TABLES	v
LIST OF FIGURES	vi
ABSTRACT	viii
CHAPTER	
1 INTRODUCTION	1
2 AXIONS	7
2.1 Introduction	7
2.2 The Strong CP Problem	7
2.3 The Axion	11
2.3.1 Introduction	11
2.3.2 The Peccei-Quinn Solution to the Strong CP Problem	11
2.3.3 The Axion Mass	15
2.3.4 The Axion Electromagnetic Coupling	19
2.4 Axions in Cosmology	21
3 DISCRETE FLOWS AND CAUSTICS IN THE GALACTIC HALO	27
3.1 Introduction	27
3.2 Existence	27
3.3 Densities	37
3.4 Discussion	39
4 HIGH RESOLUTION SEARCH FOR DARK MATTER AXIONS	41
4.1 Introduction	41
4.2 Axion Dark Matter eXperiment	42
4.3 Axion Signal Properties	45
4.4 Noise Properties	49
4.5 Removal of Systematic Effects	53
4.6 Axion Signal Search	61
4.7 Results	64
4.8 Discussion	69

5	SUMMARY AND CONCLUSION	72
	REFERENCES	74
	BIOGRAPHICAL SKETCH	79

LIST OF TABLES

<u>Table</u>		<u>page</u>
4-1	Effective power thresholds for all n -bin searches, with the frequency resolutions, b_n and corresponding maximum flow velocity dispersions, δv_n , for a flow velocity of 600 km/s.	67
4-2	Numerically calculated values of the form factor, C , and amplifier noise temperatures, T_{el} , from NRAO specifications.	67

LIST OF FIGURES

<u>Figure</u>	<u>page</u>
3-1 A 2-D slice of 6-D phase-space. The line is a cross-section of the sheet of width δv on which the dark matter particles lie prior to galaxy formation. The wiggles are the peculiar velocities due to density perturbations. When overdensities become non-linear, the sheet begins to wind up clockwise in phase-space, as shown.	30
3-2 The phase-space distribution of dark matter particles in a galactic halo at a particular time, t . The horizontal axis is the galactocentric distance, r , in units of the halo radius, R , and v is the radial velocity. Spherical symmetry has been assumed for simplicity. Particles lie on the solid line.	31
3-3 The cross-section of the tricusp ring. Each line represents a particle trajectory. The caustic surface is the envelope of the triangular feature, inside which four flows are contained. Everywhere outside the caustic surface, there are only two flows. Illustration courtesy of A. Natarajan.	33
3-4 The tricusp ring caustic. Axial symmetry has been used for illustrative purposes. Illustration courtesy of A. Natarajan.	34
4-1 Schematic diagram of the receiver chain.	45
4-2 Sketch of the ADMX detector.	46
4-3 Power distribution for a large sample of 1-bin data.	51
4-4 Power distribution for a large sample of 2-bin data.	52
4-5 Power distribution for a large sample of 4-bin data.	53
4-6 Power distribution for a large sample of 8-bin data.	54
4-7 Power distribution for a large sample of 64-bin data.	55
4-8 Power distribution for a large sample of 512-bin data.	56
4-9 Power distribution for a large sample of 4096-bin data.	57
4-10 An environmental peak as it appears in the MR search (top) and the 64-bin HR search. The unit for the vertical axis is the rms power fluctuation in each case.	58

4–11 HR filter response calibration data (512 bin average). The power has been normalized to the maximum power output.	59
4–12 Sample 4096-bin spectrum before correction for the cavity-amplifier coupling. The line is the fit obtained using the equivalent circuit model.	60
4–13 The same 4096-bin spectrum of Fig. 4–12 after correction for the cavity-amplifier coupling.	61
4–14 Illustration of the addition scheme for the 2, 4 and 8-bin searches. The numbers correspond to the data points of the 1-bin search. Numbers within the same box are bins added together to form a single datum in the n -bin searches with $n > 1$	62
4–15 97.7% confidence level limits for the HR 2-bin search on the density of any local axion dark matter flow as a function of axion mass, for the DFSZ and KSVZ $a\gamma\gamma$ coupling strengths. Also shown is the previous ADMX limit using the MR channel. The HR limits assume that the flow velocity dispersion is less than δv_2 given by Eq. (4–13).	68
4–16 97.7% confidence level limits for the HR 4-bin search on the density of any local axion dark matter flow as a function of axion mass, for DFSZ and KSVZ $a\gamma\gamma$ coupling strengths. Densities above the lines are excluded. For comparison, the predicted density of the Big Flow is also shown. The HR limits assume that the flow velocity dispersion is less than δv_2 given by Eq. (4–13).	70

Abstract of Dissertation Presented to the Graduate School
of the University of Florida in Partial Fulfillment of the
Requirements for the Degree of Doctor of Philosophy

HIGH RESOLUTION SEARCH FOR DARK MATTER AXIONS IN MILKY
WAY HALO SUBSTRUCTURE

By

Leanne Delma Duffy

August 2006

Chair: Pierre Sikivie
Major Department: Physics

The axion is one of the leading particle candidates for the universe's dark matter component. Despite possessing very small couplings, the axion's interaction with photons can be utilized to search for it using a microwave cavity detector. The Axion Dark Matter eXperiment (ADMX) uses such a detector to search for axions in our galactic halo.

ADMX has recently added a new, high resolution channel to search for axions in discrete flows. ADMX's medium resolution channel searches for axions in the thermalized component of the halo.

We review the motivation for the axion and its properties which make it a good dark matter candidate. We also review the arguments for the existence of discrete flows in galactic halos. A flow of discrete axions with small velocity dispersion will appear as a very narrow peak in the output of a microwave cavity detector. A high resolution search can detect such a peak with large signal to noise. We have performed such a search.

The details of the high resolution axion search and analysis procedure are presented. In this search, no axion signal was found in the mass range 1.98–2.17

μeV . We place upper limits on the density of axions in local discrete flows based on this result.

CHAPTER 1 INTRODUCTION

This work is on a new search for axion dark matter. The Axion Dark Matter eXperiment (ADMX) has achieved improved sensitivity by implementing a high resolution channel to search for axions in halo substructure. In this chapter, we give background information on dark matter and outline the contents of this work.

The majority of the total energy density of the universe is contributed by components that are not understood. Only approximately 4% of the energy budget is contributed by baryonic matter, that is, particles which interact electromagnetically and can thus be observed by radiation. The remaining contributions to the energy budget come from components that are called dark matter and dark energy. The dark matter component acts as matter, but interacts only gravitationally with the observable baryonic matter. This component contributes approximately 22% to the total energy density. Dark energy acts as a fluid with negative pressure and contributes the remaining 74%. The dark energy component is causing the recent epoch of accelerated expansion of the universe [1, 2]. The dark matter component is the concern of this dissertation.

Dark matter was first postulated by Fritz Zwicky in 1933 [3]. While observing the Coma cluster of galaxies, he noted that the amount of visible matter was too small for the system to be gravitationally bound. Given the observed galactic velocities, the system should fly apart. Zwicky proposed additional matter that was not visible to provide the necessary gravitational potential energy to bind the system.

The strongest evidence for dark matter today is provided by the rotation curves of spiral galaxies. Plots of observed circular velocity against radial distance

are flat to large distances. The contributions to this curve from the disk are not enough to support this rotation curve. It is thus believed that spiral galaxies consist of a visible disk embedded in a much larger elliptical dark matter halo. For a review of evidence for dark matter, see Bertone et al. [4].

Dark matter particles must have the following two properties: (1) They are effectively collisionless as far as structure formation is concerned; i.e., the only significant long-range interactions are gravitational, and (2) The dark matter must be cold; i.e., it must be non-relativistic well before the onset of galaxy formation.

The first property means that dark matter can interact only weakly with baryonic matter. The second property is necessary to form the structure in the universe that we observe today. If dark matter was more energetic, it would be able to freely stream out of the initial density perturbations that have formed into galaxies.

What the dark matter consists of is still unknown, despite knowledge of the properties it must possess. The standard model of particle physics does not contain a particle that can provide the dark matter of the universe. Extensions to the standard model do, however, provide viable particle candidates. The leading dark matter particle candidates are axions and weakly-interacting massive particles (WIMPs).

The axion is the pseudo-Nambu-Goldstone boson from the Peccei-Quinn solution to the strong CP problem [5, 6, 7, 8]. The axion mass, m_a , is constrained to lie in the range 10^{-6} to 10^{-2} eV [9, 10, 11]. There are two benchmark axion models that are minimal extensions of the standard model: the Kim-Shifman-Vainshtein-Zakharov (KSVZ) [12, 13] model and the Dine-Fischler-Srednicki-Zhitnitsy (DFSZ) [14, 15] model. In the early universe, one population of axions is produced by thermal processes and has temperature of order 1 K today. In addition, cold axion populations arise from vacuum realignment [16, 17, 18] and

string and wall decay [19, 20, 21, 22, 23, 24, 25, 26, 27, 28, 29, 30, 31]. Which mechanisms contribute depends on whether the Peccei-Quinn symmetry breaks before or after inflation. The cold axions were never in thermal equilibrium with the rest of the universe.

WIMPs are a class of dark matter candidates: heavy particles that interact via forces of weak-scale strength. WIMPs occur in many models, particularly in extensions of the standard model which include a new parity symmetry to prevent proton decay. The most popular WIMP candidate is arguably the lightest supersymmetric particle (LSP), i.e., the lightest, as-yet-undetected particle provided by the minimal supersymmetric extension to the standard model (MSSM). In contrast to axions, WIMPs are thermal relics. They began in thermal equilibrium with the primordial heat bath. When the interaction rate of WIMPs with the rest of the heat bath falls below the expansion rate of the universe, these particles decouple or “freeze out.” Their evolution is then governed by the universe’s expansion and gravitational interactions.

Much work is currently underway to detect dark matter and deduce its particle properties. ADMX is a direct detection experiment searching for dark matter axions [32, 33, 34, 35]. This experiment uses a tunable Sikivie microwave cavity [36] to search for axions. When the resonant frequency of the cavity, ν , corresponds to the energy, E_a , of axions passing through the cavity (i.e., $\nu = E_a/h$), resonant conversion of axions to photons will occur. The signal is a peak in the energy spectrum of the output from the cavity. Many direct detection experiments are also searching for WIMPs. WIMP direct detection is based on looking for nuclear recoils from the elastic scattering of passing WIMPs. Additionally, attempts are being made to detect dark matter indirectly using astrophysical signatures. These primarily focus on detecting the products of WIMP annihilations: neutrinos, positrons, anti-protons and gamma-rays.

These signals are dependent on the dark matter density. The power output from resonant axion conversion to photons is proportional to the local axion density. For WIMPs, the rate of nuclear recoil events from WIMP scattering is proportional to the local WIMP density. Also, the flux of annihilation products searched for in indirect detection is proportional to the square of the WIMP density at the site of annihilation. Thus it is necessary to make assumptions about the distribution of dark matter in our galactic halo. In particular, galactic halo substructure is of interest for dark matter detection. The presence of substructure in a galactic halo means that there will be regions of enhanced dark matter density, improving detection prospects due to the signal dependence on density.

While the power in an axion signal observed by a microwave cavity detector is proportional to the local axion density, the signal width is caused by the velocity dispersion of dark matter axions. In searching for axions, it is thus also necessary to make assumptions about their velocity distribution in the Milky Way halo. A number of models are used to guide ADMX's search. These are the isothermal model, the results from N-body simulations [37, 38] and a description of galactic halos in terms of discrete flows from late infall of dark matter onto the galaxy. A specific model which considers late infall is the caustic ring model [39, 40].

In the isothermal model, it is assumed that the dark matter halo has thermalized via virialization and thus has a Maxwell-Boltzmann velocity distribution. ADMX's medium resolution (MR) channel [34] searches for such axions, assuming that the velocity dispersion is $\mathcal{O}(10^{-3}c)$ or less, where c is the velocity of light. (The escape velocity from our galaxy is approximately $2 \times 10^{-3}c$.)

Of particular interest to this work is the existence of cold flows of dark matter axions within the halo. Such flows are associated with the tidal disruption of subhalos predicted by N-body simulations and with late infall of dark matter onto the galactic halo.

Numerical simulations indicate that hundreds of smaller clumps, or subhalos, exist within the larger halo [37, 38]. Tidal disruption of these subhalos leads to flows in the form of “tidal tails” or “streams.” The Earth may currently be in a stream of dark matter from the Sagittarius A dwarf galaxy [41, 42].

Non-thermalized flows from late infall of dark matter onto the halo are also expected [43, 44]. Dark matter that has only recently fallen into the gravitational potential of the galaxy will have had insufficient time to thermalize with the rest of the halo. This dark matter will be present in the halo in the form of discrete flows. There will be one flow of particles falling onto the galaxy for the first time, one due to particles falling out of the galaxy’s gravitational potential for the first time, one from particles falling into the potential for the second time, etc. Furthermore, where the gradient of the particle velocity diverges, particles “pile up” and form caustics. In the limit of zero flow velocity dispersion, caustics have infinite particle density. The velocity dispersion of cold axions at a time, t , prior to galaxy formation is approximately $\delta v_a \sim 3 \times 10^{-17} (10^{-5} \text{eV}/m_a) (t_0/t)^{2/3}$ [40], where t_0 is the present age of the universe. Thus, a flow of dark matter axions will have a small velocity dispersion, leading to a large, but finite density at the location of a caustic.

The caustic ring model predicts that the Earth is located near a caustic feature [45]. This model, fitted to bumps in the Milky Way rotation curve and a triangular feature seen in the IRAS maps, predicts that the flows falling in and out of the halo for the fifth time contain a significant fraction of the local halo density. The predicted densities are $1.7 \times 10^{-24} \text{ g/cm}^3$ and $1.5 \times 10^{-25} \text{ g/cm}^3$ [45], comparable to the local dark matter density of $9.2 \times 10^{-25} \text{ g/cm}^3$ predicted by Gates et al. [46]. The flow of the greatest density is referred to as the “Big Flow.”

The possible existence of discrete flows provides an opportunity to increase the discovery potential of ADMX. A discrete axion flow produces a narrow peak in the

spectrum of microwave photons in the experiment and such a peak can be searched for with higher signal-to-noise than the signal from axions in an isothermal halo. A high resolution (HR) channel has been built to take advantage of this opportunity. If a signal is found, the HR channel will also provide detailed information on the structure of the Milky Way halo.

The HR channel is the most recent addition to ADMX, implemented as a simple addition to the receiver chain, running in parallel with the MR channel. This channel and the possible existence of discrete flows can improve ADMX's sensitivity by a factor of three[35], significantly enhancing its discovery potential.

This work is arranged as follows. Background information on the axion is given in Chapter 2. The strong CP problem of the standard model of particle physics, the motivation for the axion, is described and the Peccei-Quinn solution, resulting in the axion, is discussed. Properties important to axion detection, such as its mass and coupling, are also reviewed. Some astrophysical and cosmological consequences of the axion are outlined, particularly the production of cold axion populations. A review of discrete flows and caustics in the galactic halo is presented in Chapter 3. Chapter 4 describes ADMX and provides details of the HR analysis. The new result, improving ADMX's search sensitivity by a factor of three, is also shown. A summary and conclusions are presented in Chapter 5.

CHAPTER 2 AXIONS

2.1 Introduction

The axion is the pseudo-Nambu-Goldstone boson implied by the Peccei-Quinn solution to the strong CP problem [5, 6, 7, 8]. It is also a good candidate for the dark matter of the universe. This chapter provides background information on axions. The strong CP problem is described in Section 2.2. In Section 2.3, the Peccei-Quinn solution to this problem is outlined, using the original Peccei-Quinn-Weinberg-Wilczek axion model. Axions are shown to be a natural consequence of this solution. Axion properties important to detection are also reviewed. Section 2.4 discusses cosmological aspects of axions, specifically how axion dark matter arises and the limits that cosmology and astrophysics place on the axion mass.

2.2 The Strong CP Problem

Quantum chromodynamics (QCD) is the theory of the strong nuclear forces. Its gauge symmetry is $SU_C(3)$, the color symmetry group. In nature, QCD is not a stand-alone theory. It is embedded within the standard model of particle physics. The full gauge symmetry of the standard model is $SU_C(3) \times SU_L(2) \times U_Y(1)$, i.e., the direct product of the color, left-handed and hypercharge symmetries, respectively. The unified $SU_L(2) \times U_Y(1)$ forms the electroweak symmetry. Breaking of the electroweak symmetry down to $U_{EM}(1)$ via the Higgs mechanism results in the W^\pm and Z boson masses and quark and lepton masses. In this section, we outline the strong CP problem and explain that both QCD and the electroweak effects that give the quarks mass combine to create this problem.

The Lagrangian of QCD is

$$\mathcal{L}_{QCD} = -\frac{1}{4}G_{\mu\nu}^a G^{a\mu\nu} + \sum_{j=1}^N [i\bar{q}_j \gamma^\mu D_\mu q_j - (m_j q_{Lj}^\dagger q_{Rj} + \text{h.c.})] + \frac{\theta g^2}{16\pi^2} G_{\mu\nu}^a \tilde{G}^{a\mu\nu} . \quad (2-1)$$

The q_i are the quark fields, the subscript i indicating each of the $N = 6$ quark flavors and the additional subscript L or R denoting a left- or right-handed field. The m_i are the quark masses, g is the color coupling and the γ_μ are the gamma matrices. The notation ‘‘h.c.’’ stands for hermitian conjugate. The gluon field strength tensor is

$$G_{\mu\nu}^a = \partial_\mu A_\nu^a - \partial_\nu A_\mu^a - gf^{abc} A_\mu^b A_\nu^c . \quad (2-2)$$

where A_μ^a is the gluon vector potential, the superscripts referring to the eight possible gluon color assignments, and f^{abc} are the structure constants of $SU_C(3)$.

Acting on a spinor field, ψ , the covariant derivative, D_μ , is

$$D_\mu \psi = (\partial_\mu + igA_\mu^a \frac{\lambda_a}{2}) \psi , \quad (2-3)$$

where the λ_a are the Gell-Mann matrices. The final term of Eq. (2-1) is the ‘‘ θ -term.’’ The angle, θ , is a parameter and $\tilde{G}^{a\mu\nu}$ is the dual tensor to the gluon field strength, defined by

$$\tilde{G}^{a\mu\nu} = \frac{1}{2} \epsilon^{\mu\nu\rho\sigma} G_{\rho\sigma}^a , \quad (2-4)$$

with $\epsilon^{\mu\nu\rho\sigma}$, the Levi-Civita tensor.

The parameters of QCD are thus g , m_j and θ . The color coupling, g is energy dependent and in defining the theory, it is normally exchanged for the QCD confinement scale, Λ_{QCD} , of order 200 MeV. The parameter, θ , is the QCD vacuum angle. This parameter is necessary to fully describe QCD because the $SU_C(3)$ gauge symmetry is non-Abelian. Non-Abelian gauge potentials have disjoint sectors, labelled by an integer topological winding number. These sectors are disjoint as they cannot be transformed continuously into each other. There exists a

vacuum configuration corresponding to each n , between which quantum tunnelling can occur. The gauge invariant QCD vacuum state is thus a superposition of vacua of different n , i.e.,

$$|\theta\rangle = \sum_n e^{-in\theta} |n\rangle . \quad (2-5)$$

This is the origin of θ .

In the limit of massless quarks, \mathcal{L}_{QCD} has a classical chiral symmetry, $U_A(1)$. However, this symmetry is anomalous. The existence of the Adler-Bell-Jackiw anomaly [47, 48] means that this symmetry is not present in the quantum theory. In the full quantum theory, including quark masses, the physics of QCD remains unchanged under the transformations,

$$q_i \rightarrow e^{i\alpha_i\gamma_5/2} q_i \quad (2-6)$$

$$m_i \rightarrow e^{-i\alpha_i} m_i \quad (2-7)$$

$$\theta \rightarrow \theta - \sum_{i=1}^N \alpha_j . \quad (2-8)$$

While the physics remains the same, this is not a symmetry because the parameter θ has changed. The transformations of Eq. (2-6) through Eq. (2-8) can be used to move phases between the quark masses and θ . However, the quantity,

$$\bar{\theta} = \theta - \arg(m_1 m_2 \dots m_N) , \quad (2-9)$$

is invariant and therefore observable, unlike θ . This is commonly written as

$$\bar{\theta} = \theta - \arg \det \mathbf{M} , \quad (2-10)$$

where \mathbf{M} is quark mass matrix.

The θ -term violates the discrete parity symmetry (P) and the combined operation of a parity transformation followed by charge conjugation (CP). If CP was a good symmetry of the standard model, the θ -term would not be permitted.

However, this is not the case; CP violation has been observed in the electroweak sector. Consequently, there is no apparent reason why the θ -term would not be present in the standard model.

While CP violation is present in the electroweak sector of the standard model, it has not been observed in QCD. An electric dipole moment for the neutron is the most easily observed consequence of strong CP violation. The θ -term results in a neutron electric dipole moment of [9, 49, 10, 11],

$$|d_n| \sim 10^{-16} \bar{\theta} e \text{ cm} , \quad (2-11)$$

where e is the electric charge. The current experimental limit is [50]

$$|d_n| < 6.3 \times 10^{-26} e \text{ cm} , \quad (2-12)$$

thus $|\bar{\theta}| \lesssim 10^{-9}$. However, there is no reason to expect that $\bar{\theta}$ should be so close to zero. Since CP violation is introduced in the standard model by allowing the quark mass matrices to have arbitrary complex entries, θ is naturally expected to be of order one. This is the strong CP problem, i.e. the question of why the angle $\bar{\theta}$ should be nearly zero, when CP violation is present in the standard model.

A number of solutions to the strong CP problem have been proposed. The Peccei-Quinn (PQ) solution [5, 6] results in the presence of an axion [7, 8], which has the additional motivation of being a good candidate for the dark matter of the universe. This solution is outlined in detail in the following section. Other solutions include the up quark mass being zero and that CP is spontaneously broken. If the bare up quark mass is zero, the $\bar{\theta}$ dependence of the QCD Lagrangian disappears and the strong CP problem is solved. This solution is, however, disfavored by lattice calculations and by the success of first order chiral perturbation theory in reproducing the pattern of pseudo-scalar meson masses. The Nelson-Barr model is an example of a theory where the strong CP problem is solved by properly

engineered spontaneous CP violation [51, 52]. We focus on only the PQ solution in the following section.

2.3 The Axion

2.3.1 Introduction

This section provides important background information for axion detection. In Section 2.3.2, we discuss the PQ solution to the strong CP problem. The original Peccei-Quinn-Weinberg-Wilczek axion model is used for illustration, but other axion models are also discussed. A derivation of the axion mass is given in Section 2.3.3, using the methods of low energy effective theory. In Section 2.3.4, the axion-electromagnetic coupling is reviewed. This coupling is the basis for axion detection experiments. The resulting power developed in a microwave cavity detector, using this coupling, is also given.

2.3.2 The Peccei-Quinn Solution to the Strong CP Problem

The Peccei-Quinn solution to the strong CP problem promotes $\bar{\theta}$ from a parameter to a dynamical variable. To implement this mechanism, a global symmetry, $U(1)_{PQ}$, is introduced. This symmetry has a color anomaly and is spontaneously broken. The resulting pseudo-Nambu-Goldstone boson is the axion. The axion field, a , can be redefined to absorb the parameter $\bar{\theta}$. The non-perturbative effects which make QCD $\bar{\theta}$ dependent result in a potential for the axion field, causing it to relax to the CP conserving minimum and solving the strong CP problem.

To realize the PQ solution, it is necessary to add new fields to the standard model, otherwise there are no degrees of freedom available to accommodate the axion. In the original, Peccei-Quinn-Weinberg-Wilczek (PQWW) axion model an additional Higgs doublet was introduced. We review this model to demonstrate the Peccei-Quinn mechanism in this section.

The simplest way to introduce additional degrees of freedom is via an extra Higgs doublet. We assume that one of the Higgs doublets, ϕ_u , couples to the up-type quarks and the other, ϕ_d , couples to the down-type quarks. We distinguish between the up- and down-type quarks by labelling them u_i and d_i , respectively (rather than q_i , as in the previous section). As there are N quarks, there are $N/2$ up-type quarks and down-type quarks. The leptons can acquire mass through Yukawa couplings to either of the Higgs doublets or to a third Higgs doublet. We ignore this complication here and simply examine the couplings to quarks. The quarks acquire their masses from the expectation values of the neutral components of the Higgs, ϕ_u^0 and ϕ_d^0 . The mass generating couplings are

$$\mathcal{L}_m = y_i^u u_{Li}^\dagger \phi_u^0 u_{Ri} + y_i^d d_{Li}^\dagger \phi_d^0 d_{Ri} + \text{h.c.} . \quad (2-13)$$

Peccei and Quinn chose the Higgs potential to be

$$V(\phi_u, \phi_d) = -\mu_u^2 \phi_u^\dagger \phi_u - \mu_d^2 \phi_d^\dagger \phi_d + \sum_{i,j} a_{ij} \phi_i^\dagger \phi_i \phi_j^\dagger \phi_j + \sum_{i,j} b_{ij} \phi_i^\dagger \phi_j \phi_j^\dagger \phi_i , \quad (2-14)$$

where the matrices (a_{ij}) and (b_{ij}) are real and symmetric and the sum is over the two types of Higgs fields. With this choice of potential, the full Lagrangian, including the kinetic term and θ -term, has the following global invariance, $U_{PQ}(1)$:

$$\phi_u \rightarrow e^{i2\alpha_u} \phi_u \quad (2-15)$$

$$\phi_d \rightarrow e^{i2\alpha_d} \phi_d \quad (2-16)$$

$$u_i \rightarrow e^{-i\alpha_u \gamma_5} u_i \quad (2-17)$$

$$d_i \rightarrow e^{-i\alpha_d \gamma_5} d_i \quad (2-18)$$

$$\bar{\theta} \rightarrow \bar{\theta} - N(\alpha_u + \alpha_d) . \quad (2-19)$$

Note that it is possible to write down lepton couplings which also observe the PQ symmetry. It is necessary that these couplings do so, otherwise a potential term for α will result, destroying the PQ mechanism.

When the electroweak symmetry breaks, the neutral Higgs components acquire vevs:

$$\langle \phi_u^0 \rangle = v_u e^{iP_u/v_u} \quad (2-20)$$

$$\langle \phi_d^0 \rangle = v_d e^{iP_d/v_d} . \quad (2-21)$$

One linear combination of the Nambu-Goldstone fields, P_u and P_d , is the longitudinal component of the Z-boson, as per electroweak symmetry breaking in the standard model. This combination is

$$h = \cos \beta_v P_u - \sin \beta_v P_d . \quad (2-22)$$

The orthogonal combination is the axion field,

$$a = \sin \beta_v P_u + \cos \beta_v P_d . \quad (2-23)$$

Thus,

$$P_u = \sin \beta_v a + \cos \beta_v h \quad (2-24)$$

$$P_d = \cos \beta_v a - \sin \beta_v h . \quad (2-25)$$

Using Eqs. (2-20), (2-21), (2-24) and (2-25) in Eq. (2-13), the axion couplings to quarks arise from

$$-\mathcal{L}_m = m_i^u u_{Li}^\dagger e^{i \frac{\sin \beta_v}{v_u} a} u_{Ri} + m_i^d d_{Li}^\dagger e^{i \frac{\cos \beta_v}{v_d} a} d_{Ri} + \text{h.c.} , \quad (2-26)$$

where $m_i^u = y_i^u v_u$ and $m_i^d = y_i^d v_d$. The axion field dependence can be removed from the mass terms using the transformations of Eqs. (2-17), (2-18) and (2-19).

Direct couplings between the axion and quarks will still remain in the Lagrangian,

through the associated change in the quark kinetic term. The resulting change in $\bar{\theta}$ is

$$\bar{\theta} \rightarrow \bar{\theta} - N(v_u/v_d + v_d/v_u)a/v , \quad (2-27)$$

where $v = \sqrt{v_u^2 + v_d^2}$. The axion field can be redefined to absorb $\bar{\theta}$ on the right-hand side of Eq. (2-27). Defining

$$V_{PQ} = \frac{2v}{v_u/v_d + v_d/v_u} , \quad (2-28)$$

the θ -term of Eq. (2-1) is replaced by

$$\mathcal{L}_a = \frac{ag^2}{16\pi^2 V_{PQ}} G_{\mu\nu}^a \tilde{G}^{a\mu\nu} . \quad (2-29)$$

Non-perturbative QCD effects explicitly break the Peccei-Quinn symmetry, but do not become important until the universe cools to the quark-hadron transition. These effects give the axion field a potential and when they become important, the field relaxes to the minimum, which conserves CP. Hence the PQ mechanism, which replaces $\bar{\theta}$ with the dynamical axion field, solves the strong CP problem.

However, the PQWW axion has been ruled out by observation. Under the PQWW scheme, the axion mass is inherently tied to the electroweak symmetry breaking scale, v . As $V_{PQ} \sim v$ and $v = 247$ GeV, the axion mass is of the order of 100 keV. Such a heavy axion would have been observed at particle colliders and has thus been ruled out. The calculation of the axion mass is reviewed in the next subsection.

While the PQWW axion model is not viable, this does not, however, eliminate the possibility of an axion solving the strong CP problem. “Invisible” axion models, named such for their extremely weak couplings, are still possible. In an invisible axion model, the PQ symmetry is decoupled from the electroweak scale and instead is spontaneously broken at a much higher temperature, decreasing the axion mass and coupling strength. Two benchmark, invisible axion models

exist: the Dine-Fischler-Srednicki-Zhitnitsky (DFSZ) and Kim-Shifman-Vainshtein-Zhakharov (KSVZ) models. In both the KSVZ and DFSZ models, an axion with permissible mass and couplings results.

In the KSVZ model, only the Higgs doublet of the standard model occurs. The axion is introduced as the phase of an additional electroweak singlet scalar field. The known quarks cannot be directly coupled to such a field, as the Yukawa couplings would lead to unreasonably large quark masses. Instead, this scalar is coupled to an additional heavy quark, also an electroweak singlet. The axion couplings are then induced by the interactions of the heavy quark with the other fields.

The DFSZ model has two Higgs doublets, as in the PQWW model, and an additional electroweak singlet scalar. It is the electroweak singlet scalar which acquires a vev at the PQ symmetry breaking scale. The scalar does not couple directly to quarks and leptons, but through its couplings to the two Higgs doublets.

Thus, it is possible for the existence of an axion to solve the strong CP problem. While significant for that alone, the axion also provides an interesting candidate for the cold dark matter of the universe.

2.3.3 The Axion Mass

We review how the axion mass can be obtained from the low-energy effective field theory, using the chiral Lagrangian. For this purpose, we consider only the two lightest quarks, up and down. The chiral Lagrangian is invariant under $SU_L(2) \times SU_R(2) \times U_V(1)$. We will introduce an extra $U_A(1)$ symmetry, but break it explicitly by giving a large mass to the eta particle. Indeed, the group $U_A(1)$ is not actually a symmetry of QCD, as it is broken at the quantum level by instanton effects. The symmetries are spontaneously broken down to $SU_{L+R}(2) \times U_V(1)$ by the quark condensation at the quark-hadron transition. At the scale, Λ , the quark

condensate acquires expectation value

$$\langle q_{Li}^\dagger q_{Rj} \rangle_0 = -\Lambda^3 U(\boldsymbol{\pi})_j^i, \quad (2-30)$$

where $\boldsymbol{\pi}(x)$ is the pion field. The scale, Λ , is of the order of Λ_{QCD} , but not equal to it. The matrix U is given by

$$U(\boldsymbol{\pi}) = \exp\left(\frac{i\boldsymbol{\pi} \cdot \boldsymbol{\tau}}{f_\pi}\right), \quad (2-31)$$

where $\boldsymbol{\tau}$ is the Pauli matrices and f_π is the pion decay constant, equal to 93 MeV.

For the $SU_{L+R}(2)$ triplet, the pions, the effective Lagrangian is

$$\mathcal{L}_\pi = \frac{f_\pi^2}{4} \text{Tr}(\partial_\mu U^\dagger \partial^\mu U) + \Lambda^3 \text{Tr}(m_q U + \text{h.c.}), \quad (2-32)$$

where m_q is the diagonal quark mass matrix,

$$m_q = \begin{pmatrix} m_u & 0 \\ 0 & m_d \end{pmatrix}. \quad (2-33)$$

Expansion of the Lagrangian shows the pion mass to be

$$m_\pi^2 = 2\Lambda^3 \frac{m_u + m_d}{f_\pi^2}. \quad (2-34)$$

To find the axion mass, we also need to introduce the would-be Nambu-Goldstone boson associated with the spontaneous breaking of the $U_A(1)$ symmetry. We denote this particle as η (eta) in the following (this state is actually some linear combination of the η and η' pseudo-scalar mesons). The expectation value of the quark condensate becomes

$$\langle q_{Li}^\dagger q_{Rj} \rangle_0 = -\Lambda^3 U(\boldsymbol{\pi})_j^i \exp\left(\frac{i\eta}{f_\eta}\right), \quad (2-35)$$

where f_η is the η decay constant. The effective Lagrangian is

$$\begin{aligned} \mathcal{L}_{\pi,\eta} = & \frac{1}{2}\partial_\mu\eta\partial^\mu\eta + \frac{f_\pi^2}{4}\text{Tr}(\partial_\mu U^\dagger\partial^\mu U) \\ & + \Lambda^3\text{Tr}(m_q U \exp\left(\frac{i\eta}{f_\eta}\right) + \text{h.c.}) + \frac{1}{8}m_\eta^2 f_\eta^2 \cos\left(\frac{2\eta}{f_\eta}\right), \end{aligned} \quad (2-36)$$

where the final term is the potential for rotations in the $U_A(1)$ direction.

When the θ -term is included, the expectation value of the condensate remains that given in Eq. (2-35), except that $\frac{\eta}{f_\eta}$ is replaced by $\frac{\eta}{f_\eta} + \frac{\theta}{2}$. Indeed, under a $U_A(1)$ transformation,

$$q_j \rightarrow e^{i\frac{\theta}{4}\gamma_5} q_j \quad (2-37)$$

$$m_q \rightarrow e^{-i\frac{\theta}{2}} m_q \quad (2-38)$$

$$\frac{\eta}{f_\eta} \rightarrow \frac{\theta}{2} + \frac{\eta}{f_\eta}. \quad (2-39)$$

In an axion model, θ is replaced by $\theta + \frac{Na}{v_a}$, where v_a is the scale at which the PQ symmetry breaks. The constant N is defined by the anomaly,

$$N = 2 \sum_f p_f t_f, \quad (2-40)$$

where p_f is the appropriate charge and t_f is the second casimir operator of the algebra. The axion decay constant, f_a is defined by

$$f_a = \frac{v_a}{N}. \quad (2-41)$$

The effective Lagrangian, including the θ -term and the axion field, is

$$\begin{aligned} \mathcal{L}_{\pi,\eta,a} = & \frac{1}{2}\partial_\mu a\partial^\mu a + \frac{1}{2}\partial_\mu\eta\partial^\mu\eta + \frac{f_\pi^2}{4}\text{Tr}(\partial_\mu U^\dagger\partial^\mu U) \\ & + \Lambda^3\text{Tr}(m_q U \exp\left(\frac{i\eta}{f_\eta}\right) + \text{h.c.}) + \frac{1}{8}m_\eta^2 f_\eta^2 \cos\left(\frac{2\eta}{f_\eta} + \theta + \frac{Na}{v_a}\right) \end{aligned} \quad (2-42)$$

The variable θ defines the origin of the axion field, so we may choose this to be zero. The quark mass matrix can be written as a real matrix times a phase and

we may rotate to move θ onto the quark mass term. This illustrates that the θ dependence is always a dependence on $\bar{\theta}$.

The eta, neutral pion and axion fields mix, as they all have the same quantum numbers. Firstly, consider η - a mixing. The physical η field is

$$\eta_{phys} = \eta + \frac{Naf_\eta}{2v_a} \quad (2-43)$$

and we use the redefinition

$$a' = a - \frac{Nf_\eta}{2v_a} . \quad (2-44)$$

As the minimum of the potential occurs when the cosine term is zero, we may set η_{phys} to zero. The new Lagrangian is

$$\mathcal{L}_{\pi,a} = \frac{1}{2}\partial_\mu a' \partial^\mu a' + \frac{f_\pi^2}{4}\text{Tr}(\partial_\mu U^\dagger \partial^\mu U) + \Lambda^3 \text{Tr}(m_q U \exp\left(\frac{-iNa'}{2v_a}\right) + \text{h.c.}) . \quad (2-45)$$

We find that the minimum of the potential occurs at $\pi = 0$ and $a' = 0$. The physical neutral pion and axion fields are

$$\pi_{phys}^0 = \pi^0 + \frac{m_d - m_u}{m_d + m_u} \frac{f_\pi}{2f_a} a' + \mathcal{O}\left(\frac{f_\pi^2}{f_a^2}\right) \quad (2-46)$$

$$a_{phys} = a' - \frac{m_d - m_u}{m_d + m_u} \frac{f_\pi}{2f_a} \pi^0 + \mathcal{O}\left(\frac{f_\pi^2}{f_a^2}\right) , \quad (2-47)$$

with corresponding masses

$$m_{\pi^0}^2 = \Lambda^3 \frac{m_u + m_d}{f_\pi^2} + \mathcal{O}\left(\frac{f_\pi^2}{f_a^2}\right) \quad (2-48)$$

$$m_a^2 = \Lambda^3 \frac{m_u m_d}{f_a^2 (m_u + m_d)} + \mathcal{O}\left(\frac{f_\pi^2}{f_a^2}\right) \quad (2-49)$$

$$= \frac{f_\pi^2 m_\pi^2}{f_a^2} \frac{m_u m_d}{(m_u + m_d)^2} . \quad (2-50)$$

Using the standard values for m_π , f_π , m_u and m_d , the axion mass can be expressed as [9, 49, 10, 11]

$$m_a \simeq 6 \times 10^{-6} \text{ eV} \left(\frac{10^{12} \text{ GeV}}{f_a} \right) . \quad (2-51)$$

2.3.4 The Axion Electromagnetic Coupling

Axion detection is based on its electromagnetic coupling [36]. We discuss how this coupling arises in effective field theory and review the power developed in a microwave cavity experiment in this section.

The axion electromagnetic coupling is due to mixing between the axion, neutral pion and eta. The couplings of the Lagrangian for any of these particles to decay to two photons is

$$\mathcal{L}_{\pi^0/\eta/a\rightarrow\gamma\gamma} = \frac{\alpha}{4\pi} \left(\frac{\pi^0}{f_\pi} + \frac{5}{3} \frac{\eta}{f_\eta} + \frac{N_e}{2} \frac{a}{v_a} \right) F_{\mu\nu} \tilde{F}^{\mu\nu} . \quad (2-52)$$

The coefficients in the above equation arise from the trace over the anomaly loop.

The constant N_e is given by

$$N_e = 2 \sum_f p_f (e_f)^2 , \quad (2-53)$$

where p_f is the PQ charge of a right-handed quark field. Using the definition of the physical axion field given in Eqs. (2-44) and (2-47), the resulting axion coupling to two photons is

$$\mathcal{L}_{a\gamma\gamma} = g_\gamma \frac{\alpha}{4\pi} \frac{a}{f_a} F_{\mu\nu} \tilde{F}^{\mu\nu} , \quad (2-54)$$

where

$$g_\gamma = \frac{1}{2} \left(\frac{N_e}{N} - \frac{5}{3} - \frac{m_d - m_u}{m_d + m_u} \right) \quad (2-55)$$

and we have relabelled the physical axion field as a . In grand unified theories, N_e and N are related, with $N_e/N = 8/3$. In this case, $g_\gamma = 0.36$. Both the PQWW and DFSZ axion models are grand-unifiable. In the KSVZ axion model, this is not the case. The introduction of an additional heavy neutral quark means that the KSVZ axion model cannot fit within a grand unified theory. In this case, $N_e = 0$, as the up and down quarks carry no PQ charge, and $g_\gamma = -0.97$.

The full Lagrangian for the interaction of axions with photons in free space is [36]

$$\mathcal{L} = -\frac{1}{4}F_{\mu\nu}F_{\mu\nu} + g_\gamma \frac{\alpha}{4\pi} \frac{a}{f_a} F_{\mu\nu} \tilde{F}^{\mu\nu} + \frac{1}{2}\partial_\mu a \partial^\mu a - \frac{1}{2}m_a^2 a^2 \left[1 + \mathcal{O}\left(\frac{a^2}{v^2}\right) \right]. \quad (2-56)$$

In terms of the electric and magnetic fields, \mathbf{E} and \mathbf{B} , and introducing a medium with dielectric constant, ϵ , Eq. (2-56) can be written as

$$\mathcal{L} = \frac{1}{2}(\epsilon E^2 - B^2) + \frac{1}{2}\partial_\mu a \partial^\mu a - \frac{1}{2}m_a^2 a^2 - g_\gamma \frac{\alpha}{4\pi} \frac{a}{f_a} \mathbf{E} \cdot \mathbf{B} \quad (2-57)$$

In a cavity permeated by a strong, inhomogeneous magnetic field, resonant conversion of axions to photons can be induced if the cavity frequency corresponds to that of the axion energy. The resulting power developed in a microwave cavity detector is

$$P = \left(\frac{\alpha g_\gamma}{\pi f_a} \right)^2 \frac{V B_0^2 \rho_a C}{m_a} \min(Q, Q_a). \quad (2-58)$$

where V is the cavity volume, B_0 is the magnetic field strength, ρ_a is the local density of axions with energy corresponding to the cavity frequency, Q is the quality factor of the cavity and Q_a is the ratio of the energy of halo axions to their energy spread, equivalent to a “quality factor” for the halo axion signal. The mode-dependent form factor, C , is given by

$$C = \frac{|\int_V d^3x \mathbf{E}_\omega \cdot \mathbf{B}_0|^2}{B_0^2 V \int_V d^3x \epsilon |\mathbf{E}_\omega|^2}, \quad (2-59)$$

in which $\mathbf{E}_\omega(\mathbf{x})$ is the time-dependent electric field of the mode under consideration and ϵ is the dielectric constant of the medium insided the cavity. This is more conveniently expressed as

$$P = 0.5 \times 10^{-21} \text{W} \left(\frac{V}{500\text{L}} \right) \left(\frac{B_0}{7\text{T}} \right)^2 C \left(\frac{g_\gamma}{0.36} \right)^2 \left(\frac{\rho_a}{0.5 \times 10^{-24} \text{g.cm}^{-3}} \right) \times \left(\frac{\nu_a}{1\text{GHz}} \right) \left(\frac{\min[Q, Q_a]}{10^5} \right), \quad (2-60)$$

where ν_a is the axion energy frequency.

Thus, when such a cavity is tuned to the correct frequency, resonant conversion of axions to photons results. This conversion is observed as a peak in the frequency spectrum of the detector output.

2.4 Axions in Cosmology

Axions may play an important role in cosmology. We focus on two aspects of this here. Firstly, for a mass in the range 10^{-6} – 10^{-4} eV, the axion is an interesting dark matter candidate. Secondly, we outline the restrictions that cosmology and astrophysics place on the axion mass and coupling.

Axions satisfy the two criteria necessary for cold dark matter: (1) a non-relativistic population of axions could be present in our universe in sufficient quantities to provide the required dark matter energy density and (2) they are effectively collisionless, i.e., the only significant long-range interactions are gravitational. There are three mechanisms via which cold axions are produced: vacuum realignment [16, 17, 18], string decay [19, 20, 21, 22, 23, 24, 25, 26, 27, 28, 29] and domain wall decay [29, 30, 31]. We discuss the history of the axion field as the universe expands and cools to see how and when these mechanisms occur. We also review the process of vacuum realignment in detail, as there will always be a contribution to the cold axion populations from that mechanism and, as discussed below, it is possible that this provides the only contribution.

There are two important scales in the problem of axions as dark matter. The first is the temperature at which the PQ symmetry breaks, T_{PQ} . Which of the above mechanisms contribute significantly to the cold axion population depends on whether this temperature is greater or less than the inflationary reheating temperature, T_R . The second is the temperature at which the axion mass, arising from non-perturbative QCD effects, becomes significant. At high temperatures, the latter effects are not significant and the axion mass is negligible [53]. The axion

mass becomes significant at a critical time, t_1 , when $m_a t_1 \sim 1$ [16, 17, 18]. The corresponding temperature is $T_1 \simeq 1$ GeV.

At initial early times, the PQ symmetry is unbroken. At T_{PQ} , it breaks spontaneously and the axion field, which is proportional to the phase of the complex scalar field acquiring a vev, may have any value. The phase varies continuously, changing by order one from one horizon to the next. Axion strings appear as topological defects. If $T_{PQ} > T_R$, the axion field is homogenized over huge distances and the string density is diluted by inflation, to the point where it is extremely unlikely that any axion strings remain in our visible universe. In the case $T_{PQ} < T_R$, the axion field is not homogenized and strings radiates cold, massless axions until non-perturbative QCD effects become significant. At this time, the axion strings become the boundaries of N domain walls. If $N = 1$, the walls bounded by string rapidly radiate cold axions and decay (domain wall decay). For $N > 1$, the domain wall problem occurs [54] because the vacuum is multiply degenerate and there is at least one domain wall per horizon. The domain walls end up dominating the energy density and cause the universe to expand as $S \propto t^2$, where S is the scale factor. Although other solutions to the domain wall problem have been proposed [29], we assume here that $N = 1$ or $T_{PQ} > T_R$. Thus, if $T_{PQ} < T_R$, string and wall decay contribute to the axion energy density. If $T_R < T_{PQ}$, and the axion string density is diluted by inflation, these mechanisms do not contribute significantly to the density of cold axions. Then, only vacuum realignment will contribute a significant amount.

Vacuum realignment will result in a population of cold axions, independent of T_R . This is discussed in more detail below, however, an overview is as follows. At T_{PQ} , the axion field amplitude may have any value. If $T_{PQ} > T_R$, the homogenization from inflation will result in a single value of the axion field over our visible universe. Non-perturbative QCD effects cause a potential for the axion field. When

these effects become significant, the axion field will begin to oscillate in the potential. These oscillations do not decay and contribute to the local energy density as non-relativistic matter. Thus, a cold axion population results from vacuum realignment, regardless of the inflationary reheating temperature.

To understand the contribution from vacuum realignment, consider a toy axion model with one complex scalar field, $\phi(x)$, in addition to the standard model fields. Let the potential for $\phi(x)$ be

$$V(\phi) = \frac{\lambda}{4} (|\phi|^2 - v_a^2)^2, \quad (2-61)$$

When the universe cools to a temperature $T_{PQ} \sim v_a$, ϕ acquires a vacuum expectation value,

$$\langle \phi \rangle = v_a \exp(i\alpha(x)). \quad (2-62)$$

The axion field is related to $\alpha(x)$, the phase of the scalar field, $\phi(x)$, by

$$a(x) \equiv v_a \alpha(x). \quad (2-63)$$

At $T \sim \Lambda$, non-perturbative QCD effects give the axion a mass. They produce an effective potential

$$\tilde{V}(\bar{\theta}) = m_a^2(T) \frac{v_a^2}{N^2} (1 - \cos \bar{\theta}), \quad (2-64)$$

where [53]

$$m_a(T) \simeq 0.1 m_a \left(\frac{\Lambda_{QCD}}{T} \right)^{3.7}. \quad (2-65)$$

The minimum of the potential occurs at

$$\bar{\theta}(x) = N\alpha(x) = 0. \quad (2-66)$$

The axion acquires mass, m_a , due to the curvature of the potential at this minimum. Given the definition of the axion field in Eq. (2-63), the effective Lagrangian

is

$$\mathcal{L} = \frac{1}{2} \partial_\mu a \partial^\mu a - m_a^2(T) \frac{v_a^2}{N^2} \left(1 - \cos \left(\frac{Na}{v_a} \right) \right) . \quad (2-67)$$

In a Friedmann-Robertson-Walker universe, the equation of motion is

$$\ddot{\alpha} + 3H(t)\dot{\alpha} - \frac{1}{R^2(t)} \nabla^2 \alpha + \frac{1}{N} m_a^2(T(t)) \sin(N\alpha) = 0 \quad (2-68)$$

Near the potential minima,

$$\tilde{V}(\alpha) \simeq \frac{1}{2} m_a^2 v_a^2 \alpha^2 , \quad (2-69)$$

and thus,

$$\sin(N\alpha) \simeq N\alpha . \quad (2-70)$$

We now restrict the discussion to the zero momentum mode. For $T_{PQ} > T_R$, this will be the only mode with significant occupation, so the final energy density calculated will be for this case. In the case, $T_R > T_{PQ}$, higher modes will also be occupied. For the zero momentum mode, the equation of motion reduces to

$$\ddot{\alpha} + 3H(t)\dot{\alpha} + m_a^2(t)\alpha = 0 , \quad (2-71)$$

i.e., the field satisfies the equation for a damped harmonic oscillator with time-dependent parameters. As no initial value of α is preferred, the most general solution is

$$\alpha = \alpha_1 + \alpha_2 t^{-\frac{1}{2}} , \quad (2-72)$$

where α_1 and α_2 are constants. Thus, at $T \gg T_{QCD}$, α is approximately constant. The field will, however, begin to oscillate in its potential when the universe cools to the critical temperature, T_1 , defined by [55]

$$m_a(T_1(t_1)) \sim 3H(T_1(t_1)) = \frac{3}{2t_1} . \quad (2-73)$$

As the axion field can realign only as fast as causality permits, the corresponding momentum of a quantum of the axion field is

$$p_a(t_1) \sim \frac{1}{t_1} \sim 10^{-9} \text{eV} \quad (2-74)$$

for $t_1 \sim 2 \times 10^{-7}$ s, i.e. the age of the universe at which the quark-hadron transition occurs. As discussed below, the axion mass is restricted to the range 10^{-6} – 10^{-2} eV and thus this population is non-relativistic or cold.

This mechanism can produce a sufficient quantity of cold axions to provide the dark matter of the universe. We show this by reviewing the energy density of axions produced by the realignment mechanism. The energy density for a homogeneous scalar field around its potential minimum is

$$\rho = \frac{v_a^2}{2} [\dot{\alpha}^2 + m_a^2(t) \alpha^2]. \quad (2-75)$$

By the Virial theorem,

$$\langle \dot{\alpha}^2 \rangle = m^2 \langle \alpha^2 \rangle = \frac{\rho}{v_a^2}. \quad (2-76)$$

As axions are non-relativistic and decoupled,

$$\rho \propto \frac{m_a(t)}{R^3(t)}. \quad (2-77)$$

Thus, the number of axions per comoving volume is conserved, provided the axion mass varies adiabatically.

The initial energy density in the coherent oscillations is

$$\rho_1 = v_a^2 m_a(t_1) \alpha_1^2 / 2 \quad (2-78)$$

$$= \frac{1}{2} f_a^2 m_a(t_1) \left(\frac{\alpha_1}{N} \right)^2. \quad (2-79)$$

The energy density in axions today is

$$\rho_0 = \frac{m_a(t_0) S^3(t_1)}{m_a(t_1) S^3(t_0)} \quad (2-80)$$

$$= \frac{1}{2} f_a^2 \frac{1}{t_1} m_a \left(\frac{S^3(t_1)}{S^3(t_0)} \right) \left(\frac{\alpha_1}{N} \right)^2, \quad (2-81)$$

where $S(t)$ is the scale factor at time, t . Eq. (2-81) implies the axion energy density,

$$\Omega_a \simeq 0.15 \left(\frac{f_a}{10^{12} \text{GeV}} \right)^{\frac{7}{6}} \alpha_1^2. \quad (2-82)$$

As the axion couplings are very small, these coherent oscillations do not decay and make a good candidate for the dark matter of the universe.

The mass is related to the Peccei-Quinn decay constant, f_a , by Eq. (2-51) and the couplings of the axion mass are inversely proportional to f_a . Thus limits on any of the axion mass, axion couplings or PQ decay constant is also a restriction on the other two. Since $\Omega_a < \Omega_{CDM} = 0.22$, $f_a < 10^{12}$ GeV and thus, $m_a > 10^{-6}$ eV. This is the lower bound on the axion mass range. If the axion mass were any greater, too much dark matter would be produced via the realignment mechanism.

The upper limit on the axion mass is 10^{-2} eV, from observations of SN1987a. The number of neutrinos observed on Earth due to this supernovae and its duration are in good agreement with models of supernovae. Light particles, such as axions, present novel cooling mechanisms that can alter the duration of supernovae. If the axion mass is less than 10^{-2} eV, axions are not produced in significant numbers to affect supernovae. However, for a range of axion masses above this, axion production and escape from supernovae will significantly shorten the supernova duration by efficiently transporting energy away. Above approximately 0.5 eV, the mean free path of an axion will be too short for significant numbers of axions to escape from supernovae. At this point, other astrophysical processes, such as the lifetime of red giants forbid axion masses in higher ranges [11].

CHAPTER 3 DISCRETE FLOWS AND CAUSTICS IN THE GALACTIC HALO

3.1 Introduction

ADMX's high resolution channel searches for discrete flows of cold axions passing the detector. As discussed in the introduction, such flows occur due to tidal stripping of dwarf galaxies and late infall of dark matter onto the galactic halo. In this chapter, we review the arguments why such flows are expected to occur in cold dark matter cosmology, thus providing an interesting possibility to search for axions.

In Section 3.2, we review literature demonstrating that discrete flows are a natural consequence of a cold dark matter cosmology. Section 3.3 discusses the densities of such flows. A significant fraction of the local halo density should be contained in discrete flows, which is important when searching for them, as the signal observed is proportional to the density. A brief discussion of evidence for flows and detection of axions in these flows concludes this chapter, in Section 3.4.

3.2 Existence

This work demonstrates that searching for discrete flows of cold axions in the galactic halo improves the sensitivity of a microwave cavity detector. However, it is necessary that such halo substructure exists for us to benefit from this improved detector sensitivity. Natarajan and Sikivie have shown that discrete flows and caustics are a necessary consequence of cold dark matter cosmology. In this section, we review the arguments for the presence of discrete flows and caustics in the galactic halo. First, we describe why it is expected that such halo substructure forms and then we review the mathematical proof for the existence of both inner and outer caustics in galactic halos.

While we are interested in this substructure from the point of view of axion detection, it should be noted that the existence of discrete flows and caustics is independent of the type of cold dark matter. The only requirement for flows and caustics to form is the assumption of cold dark matter itself. Cold dark matter particles are assumed to possess the following properties:

(1) The particles must be collisionless, i.e., the only significant interactions of these particles are gravitational. This property explains why the particles are dark matter.

(2) The particles have negligible initial velocity dispersion, where the initial conditions are those when the dark matter first falls into a galaxy's gravitational potential. This is discussed further in the following.

The primordial velocity dispersion of both axions and WIMPs is negligible [56] as far as large scale structure formation is concerned. For WIMPs, the primordial velocity dispersion is determined by the temperature, T_D , at which they decouple from the primordial heat bath. Considering Hubble expansion to be the only significant effect to alter the WIMP velocity dispersion, the velocity dispersion, δv_W , of a WIMP of mass m_W falling into a galaxy today is

$$\delta v_W \sim \left(\frac{2T_D}{m_W} \right)^{\frac{1}{2}} \left(\frac{S(t_D)}{S(t_0)} \right), \quad (3-1)$$

where S is the scale factor, given at the time of decoupling, t_D , and today, t_0 . For a WIMP with mass of 1 GeV that decoupled when the temperature was 10 MeV, the velocity dispersion today is $\delta v_W \sim 10^{-12}$.

For axions, the primordial velocity dispersion is due to the inhomogeneities in the axion field when the axion mass, m_a , becomes significant, i.e., when $m_a \sim H$ at temperature $T_a \sim 1$ GeV and time $t_a \sim 2 \times 10^{-7}$ s. The magnitude of the field inhomogeneity depends on whether the Peccei-Quinn (PQ) symmetry breaks before or after inflationary reheating. If the PQ symmetry is broken after reheating, the

axion field is inhomogeneous on the scale of the horizon size ($\sim t_1$) when the mass becomes significant and hence,

$$\delta v_a \sim \frac{1}{m_a t_1} \left(\frac{S(t_a)}{S(t_0)} \right) \sim 10^{-17} \times \left(\frac{10^{-5} \text{eV}}{m_a} \right). \quad (3-2)$$

If the PQ symmetry is broken before reheating, inflation homogenizes the axion field over enormous distances and the velocity dispersion, δv_a , due to quantum mechanical fluctuations in the axion field, is even smaller than in Eq. (3-2).

The primordial velocity dispersion of dark matter particles falling onto a galaxy at any time, t , can be obtained by substitution of $S(t_0)$ for the scale factor, $S(t)$. For both axions and WIMPs, we see that the initial velocity dispersion is so small as to be negligible.

The formation of discrete flows and caustics can be understood by considering the phase-space distribution of dark matter particles falling into a gravitational potential. At early times, prior to the onset of galaxy formation, these particles will lie on a thin 3-dimensional (3D) sheet in 6D phase-space, as illustrated in Fig. 3-1. The thickness of the sheet is proportional to the local velocity dispersion of the dark matter particles, δv , and thus the sheet is thin. This sheet will also be continuous, as the number density of particles is very large over the scale at which the sheet is bent in phase space.

As dark matter particles are collisionless, the evolution of the sheet is determined by the influence of gravity only. Where density perturbations become non-linear, the 3D sheet will begin to “wind up” clockwise in phase-space. Whereas previously, in the linear regime, the sheet covered physical space only once, it will now begin to cover physical space multiple times. After much time, the phase-space particle distribution will look as shown in Fig. 3-2. As particles fall into a gravitational potential, there will be a number of discrete flows present at each point at any time [43]. There will be one flow of particles falling in for the first time,

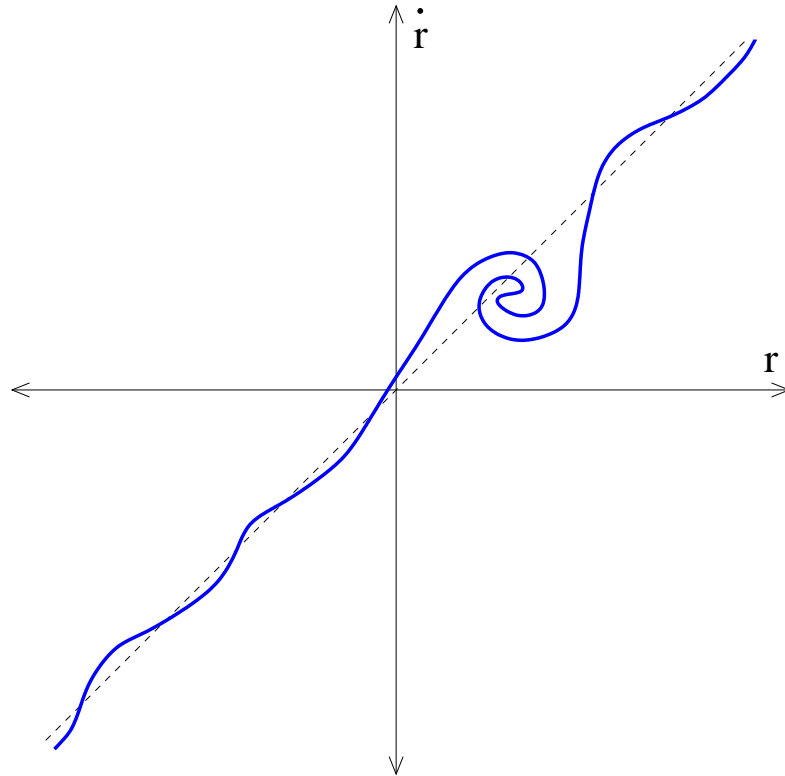


Figure 3–1. A 2-D slice of 6-D phase-space. The line is a cross-section of the sheet of width δv on which the dark matter particles lie prior to galaxy formation. The wiggles are the peculiar velocities due to density perturbations. When overdensities become non-linear, the sheet begins to wind up clockwise in phase-space, as shown.

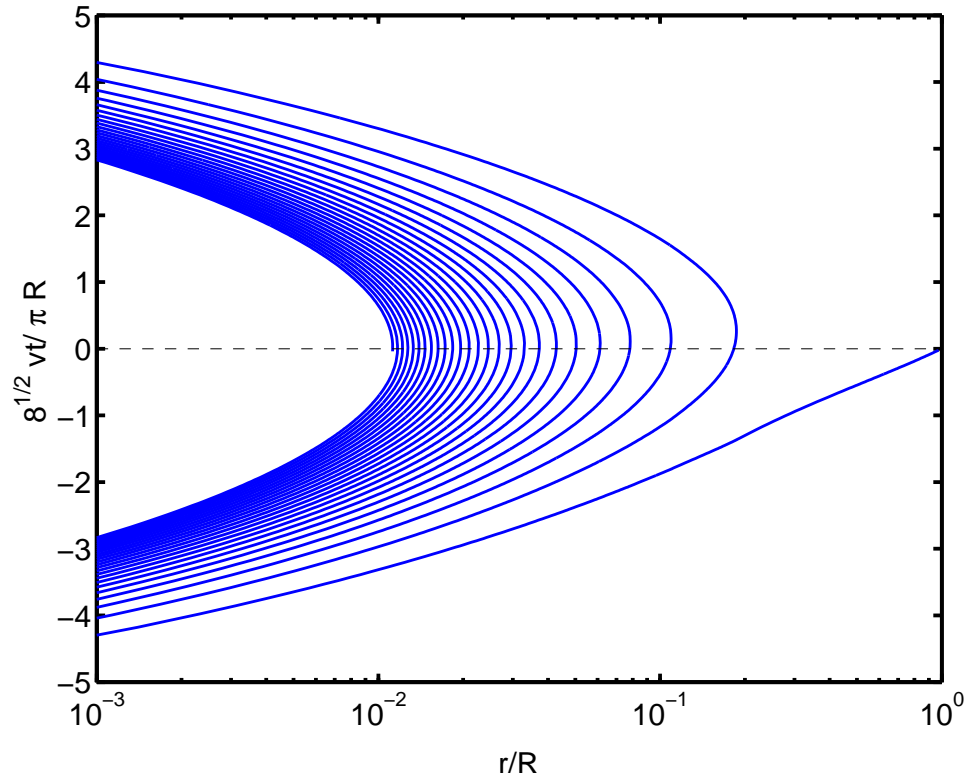


Figure 3–2. The phase-space distribution of dark matter particles in a galactic halo at a particular time, t . The horizontal axis is the galactocentric distance, r , in units of the halo radius, R , and v is the radial velocity. Spherical symmetry has been assumed for simplicity. Particles lie on the solid line.

one flow of particles falling out for the first time, one of particles falling out for the second time, etc. Also, at the locations where the sheet folds, caustics form. There are two types of caustics that occur within a galactic halo: “outer” and “inner.” Outer caustics form near where a flow of particles falling out of the halo’s gravitational potential turnaround and fall back in. These caustics are topologically spheres. Inner caustics form where particles falling into the potential reach their distance of closest approach to the center of the galaxy. When the initial velocity of infalling particles is dominated by a rotational component, inner caustics are a “tricuspid ring” [40], whose cross-section is a D_{-4} catastrophe. The cross-section is illustrated in Fig. 3-3 and the ring shown in Fig. 3-4. Axial symmetry has been used in these figures, but is not a necessary condition for the formation of caustics.

We proceed to review the mathematical arguments for the existence of outer and inner caustics [44]. Parametrize the particles on the phase-space sheet using $\boldsymbol{\alpha} = (\alpha_1, \alpha_2, \alpha_3)$. This parametrization may be chosen as convenient. Let $\mathbf{x}(\boldsymbol{\alpha}; t)$ be the physical position of the particle labelled $\boldsymbol{\alpha}$ at time t . At early times, before galactic evolution becomes non-linear, the mapping $\boldsymbol{\alpha} \rightarrow \mathbf{x}$ will be one-to-one. At late times, when the sheet covers physical space multiple times, for any given physical location \mathbf{r} there will be, in general, multiple solutions $\boldsymbol{\alpha}_j(\mathbf{r}, t)$ with $j = 1, 2, \dots, n(\mathbf{r}, t)$, to $\mathbf{r} = \mathbf{x}(\boldsymbol{\alpha}; t)$. That is, there will be particles with different $\boldsymbol{\alpha}$ at the same physical location, \mathbf{r} . The number of flows at \mathbf{r} at time t is $n(\mathbf{r}, t)$. The number density of particles on the sheet is $\frac{d^3 N}{d\alpha^3}$. It follows that the mass density in physical space is [40]

$$\rho(\mathbf{r}, t) = m \sum_{j=1}^{n(\mathbf{r}, t)} \frac{d^3 N}{d\alpha^3}(\boldsymbol{\alpha}) \frac{1}{|D(\boldsymbol{\alpha}, t)|} \Bigg|_{\boldsymbol{\alpha}=\boldsymbol{\alpha}_j(\mathbf{r}, t)} . \quad (3-3)$$

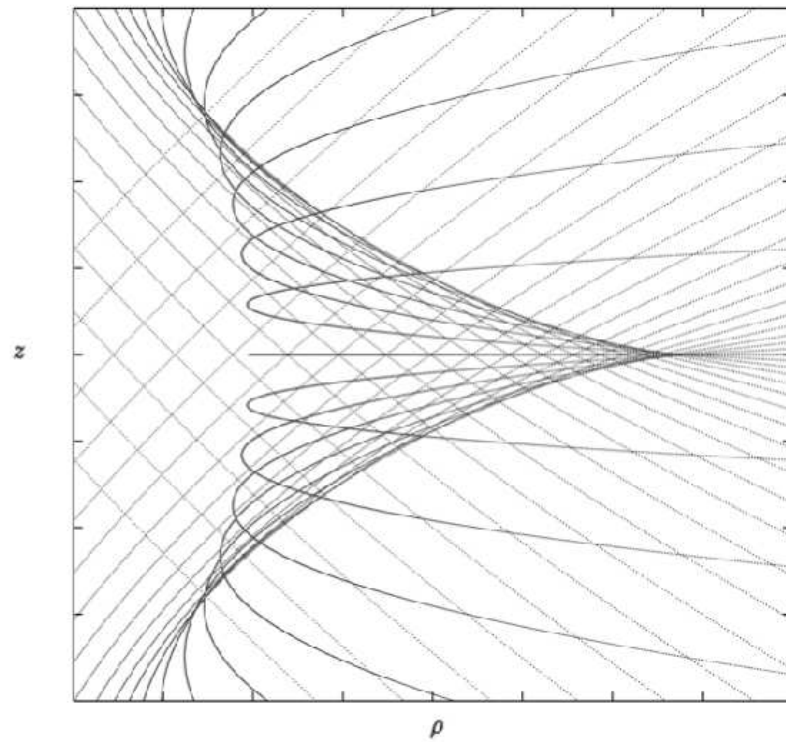


Figure 3–3. The cross-section of the tricuspid ring. Each line represents a particle trajectory. The caustic surface is the envelope of the triangular feature, inside which four flows are contained. Everywhere outside the caustic surface, there are only two flows. Illustration courtesy of A. Natarajan.

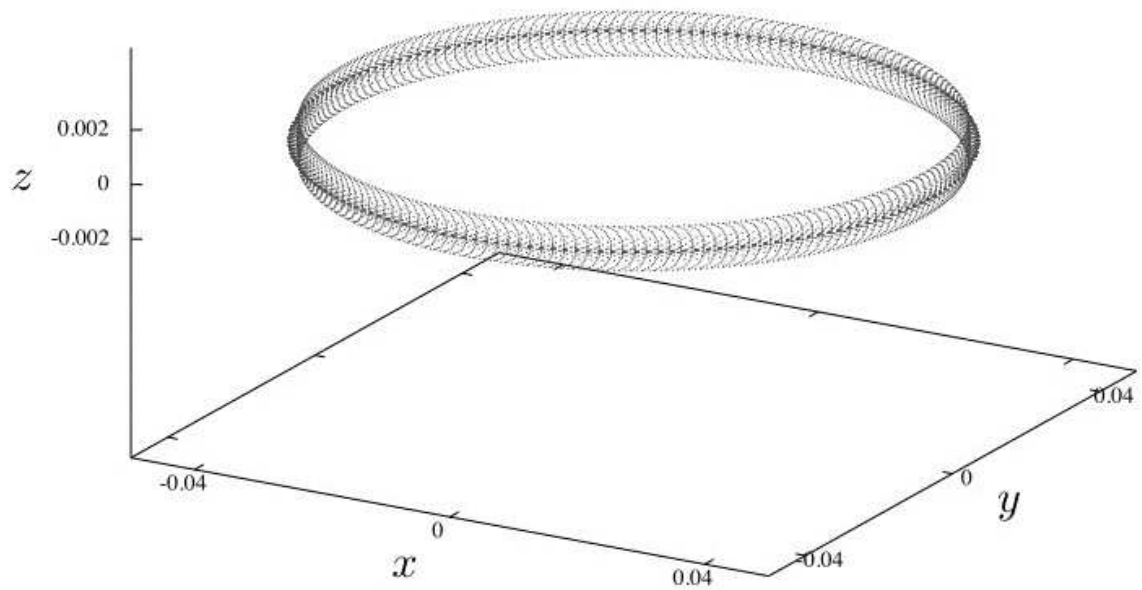


Figure 3–4. The tricusp ring caustic. Axial symmetry has been used for illustrative purposes. Illustration courtesy of A. Natarajan.

where m is the particle mass and

$$D(\boldsymbol{\alpha}, t) = \det \left(\frac{\partial \mathbf{x}(\boldsymbol{\alpha}, t)}{\partial \boldsymbol{\alpha}} \right). \quad (3-4)$$

The magnitude of D is the Jacobian of the map $\boldsymbol{\alpha} \rightarrow \mathbf{x}$. Eq. (3-3) is the sum over the mass density in each discrete flow at \mathbf{r} .

Caustics occur where $D = 0$ and the map is singular [39]. At these points, the mapping from phase-space to physical space changes from n -to-one to $(n \pm 2)$ -to-one. The physical density at the location of caustics becomes very large, as the phase-space sheet is tangent to velocity space. In the limit of zero initial velocity dispersion, the dark matter particle density diverges at the location of a caustic. In reality, these flows will have a small velocity dispersion and thus the caustics will have a large, but finite, density.

The presence of outer caustics is easily seen from Fig. 3-2. Natarajan and Sikivie [44] demonstrated that inner caustics must also be present in the galactic halo. Consider a continuous flow of cold dark matter particles falling in and out of a gravitational potential and a spherical surface of radius R surrounding the potential well. Using the parametrization, $\boldsymbol{\alpha} = (\theta, \phi, \tau)$, where θ and ϕ are the polar coordinates where a particle falling into the potential crosses the sphere at time, τ . Then $\mathbf{x}(\theta, \phi, \tau; t)$ gives the particle's position at time, t . Natarajan and Sikivie demonstrated that

$$D = \det \frac{\partial(x, y, z)}{\partial(\theta, \phi, \tau)} = \frac{\partial \mathbf{x}}{\partial t} \cdot \left(\frac{\partial \mathbf{x}}{\partial \phi} \times \frac{\partial \mathbf{x}}{\partial \theta} \right) \quad (3-5)$$

vanishes at at least one point inside the sphere at any t . Thus, a caustic is present within the sphere. Such a caustic is an inner caustic. We review their proof in the following. The variable t will be suppressed.

For each (θ, ϕ) , the time at which a particle within the sphere crossed its surface lies in the range $\tau_{out}(\theta, \phi) < \tau < \tau_{in}(\theta, \phi)$, where $\tau_{in}(\tau_{out})$ is the initial

crossing time of particles currently crossing the sphere on the way in(out). The sphere's center is chosen to lie at the origin, $\mathbf{x} = 0$. The distance from the sphere's center to a particle's position is

$$r(\theta, \phi, \tau) = \sqrt{\mathbf{x}(\theta, \phi, \tau) \cdot \mathbf{x}(\theta, \phi, \tau)} \quad (3-6)$$

and

$$\left. \frac{\partial r}{\partial \tau} \right|_{\theta, \phi, \tau_{out}(\theta, \phi)} < 0 \quad \text{and} \quad \left. \frac{\partial r}{\partial \tau} \right|_{\theta, \phi, \tau_{in}(\theta, \phi)} > 0. \quad (3-7)$$

Thus, for all (θ, ϕ) there exists a $\tau_0(\theta, \phi)$ such that

$$r(\theta, \phi, \tau_0(\theta, \phi)) = \min r(\theta, \phi, \tau) \equiv r_{min}(\theta, \phi), \quad (3-8)$$

where the minimum is over τ for fixed (θ, ϕ) . The distance $r_{min}(\theta, \phi)$ is the smallest distance to the origin among all particles labelled (θ, ϕ) .

There are two cases to be considered: $r_{min}(\theta, \phi) \neq 0$ for some (θ, ϕ) and $r_{min}(\theta, \phi) = 0$ for all (θ, ϕ) . In the first case,

$$\left. \frac{\partial r}{\partial \tau} \right|_{\theta, \phi, \tau_0(\theta, \phi)} = \frac{\mathbf{x}}{r} \cdot \left. \frac{\partial \mathbf{x}}{\partial \tau} \right|_{\theta, \phi, \tau_0(\theta, \phi)} = 0 \quad (3-9)$$

for all (θ, ϕ) such that $r_{min}(\theta, \phi) \neq 0$. The distance $r_{min}(\theta, \phi)$ has a maximum value over the sphere $S_2(\theta, \phi)$. Choose (θ_0, ϕ_0) be such that $r_{min}(\theta_0, \phi_0) = \max r_{min}(\theta, \phi)$.

Then

$$\left. \frac{\partial r}{\partial \theta} \right|_{\boldsymbol{\alpha}_0} = \frac{\mathbf{x}}{r} \cdot \left. \frac{\partial \mathbf{x}}{\partial \theta} \right|_{\boldsymbol{\alpha}_0} = 0 \quad (3-10)$$

and

$$\left. \frac{\partial r}{\partial \phi} \right|_{\boldsymbol{\alpha}_0} = \frac{\mathbf{x}}{r} \cdot \left. \frac{\partial \mathbf{x}}{\partial \phi} \right|_{\boldsymbol{\alpha}_0} = 0, \quad (3-11)$$

where $\boldsymbol{\alpha}_0 \equiv (\theta_0, \phi_0, \tau_0(\theta_0, \phi_0))$ and $\mathbf{x}(\boldsymbol{\alpha}_0) \neq 0$. Eqs. (3-9), (3-10) and (3-11) imply that $\left. \frac{\partial \mathbf{x}}{\partial \theta} \right|_{\boldsymbol{\alpha}_0}$, $\left. \frac{\partial \mathbf{x}}{\partial \phi} \right|_{\boldsymbol{\alpha}_0}$ and $\left. \frac{\partial \mathbf{x}}{\partial \tau} \right|_{\boldsymbol{\alpha}_0}$ are all perpendicular to \mathbf{x}_0 , i.e. these three vectors are linearly dependent and $D(\boldsymbol{\alpha}_0) = 0$. Thus, \mathbf{x}_0 is the location of a caustic. As

\mathbf{x}_0 depends on the choice of origin, such a caustic is spatially extended, which is as expected; caustics are generically surfaces.

In the special case, $r_{min}(\theta, \phi) = 0$ for all (θ, ϕ) , $\mathbf{x}(\theta, \phi, \tau_0(\theta, \phi)) = 0$ for all (θ, ϕ) and thus, for τ near $\tau_0(\theta, \phi)$:

$$\mathbf{x}(\theta, \phi, \tau) = \boldsymbol{\nu}(\theta, \phi)(\tau - \tau_0(\theta, \phi)) + \mathcal{O}((\tau - \tau_0(\theta, \phi))^2), \quad (3-12)$$

where

$$\boldsymbol{\nu}(\theta, \phi) = \left. \frac{\partial \mathbf{x}}{\partial \tau} \right|_{\theta, \phi, \tau_0(\theta, \phi)}. \quad (3-13)$$

Using the reparametrization, $\theta' = \theta$, $\phi' = \phi$ and $\tau' = \tau - \tau_0(\theta, \phi)$ and relabelling, $(\theta', \phi'; \tau') \rightarrow (\theta, \phi; \tau)$,

$$\mathbf{x}(\theta, \phi, \tau) = \boldsymbol{\nu}(\theta, \phi)\tau + \mathcal{O}(\tau^2). \quad (3-14)$$

Hence,

$$D(\theta, \phi, \tau) = \boldsymbol{\nu}(\theta, \phi) \cdot \left(\frac{\partial \boldsymbol{\nu}}{\partial \theta} \times \frac{\partial \boldsymbol{\nu}}{\partial \phi} \right) \tau^2. \quad (3-15)$$

As $D = 0$ at $\tau = 0$, the origin is the location of a caustic in this special case. In this case, the caustic has collapsed to a point.

Thus, both inner and outer caustics must be present in a galactic halo. Discrete flows and caustics are a natural consequence of a cold dark matter cosmology.

3.3 Densities

In order to be detectable by a microwave cavity experiment, flows in the galactic halo must have sufficient density. In this section, we review arguments that demonstrate that discrete flows are expected to contain a significant fraction of the local dark matter density. In particular, the flow density is enhanced near the location of a caustic. Evidence suggests that the Earth is located near a caustic feature.

The local density of the first few flows was first estimated by Sikivie and Ipser [43], for cases both without and with angular momentum. We review their estimates below.

The initial estimate was calculated for the first flow, i.e., the flow of particles passing Earth for only the first time. These particles had a maximum galactocentric distance of $r_m \sim 1$ Mpc, which was reached 5×10^9 years ago. The density at this location is estimated to be the average cosmological dark matter density today, $\rho_{CDM}(t_0)$. In the case of no angular momentum, the local density of the first flow will be the density at r_m multiplied by the appropriate geometrical focussing factor, i.e., $(r_m/r_\odot)^2$, thus,

$$\rho_1(r_\odot, t_0) \sim \rho_{CDM}(t_0) \left(\frac{r_m}{r_\odot} \right)^2 \sim 10^{-25} \text{g/cm}^3 . \quad (3-16)$$

When angular momentum is included, not all particles falling into the galaxies will pass through the center. Defining d as the average distance of closest approach for particles falling in for the first time, the estimated density is

$$\rho_1(r_\odot, t_0) \sim \rho_{CDM}(t_0) \left(\frac{r_m}{d} \right)^2 \sim \left(\frac{r_\odot}{d} \right)^2 10^{-25} \text{g/cm}^3 . \quad (3-17)$$

The more detailed calculations of Sikivie, Tkachev and Wang [57] confirm this estimate and provide estimates of densities of the same order of magnitude for the other flows. Their calculations show that each of the first eight in and out flows have densities of the order of 2% of the local halo density (assuming a local dark matter density of $9.2 \times 10^{-25} \text{g/cm}^3$ [46]). Thus, these estimates lead us to expect that flows contain a significant fraction of the local dark matter density.

At the location of a caustic, the dark matter density will be greatly enhanced. This will be reflected by rising bumps in the galactic rotation curve at these locations. Fitting the caustic ring model to rises in the Milky Way rotation curve and to a triangular feature in the IRAS map predicts that the flows falling in

and out for the fifth time contain a significant fraction of the halo density at the location of our solar system. The predicted densities are 1.7×10^{-24} g/cm³ and 1.5×10^{-25} g/cm³ [45]. The flow of the greatest density is called the “Big Flow.” This flow is predicted to have a velocity dispersion of 53 m/s and velocity of approximately 300 km/s relative to the Sun. Thus this flow is of particular interest for axion dark matter detection.

3.4 Discussion

In this section, we discuss evidence for discrete flows and caustics and the consequences for microwave cavity detection of axion dark matter.

As demonstrated in Section 3.2, discrete flows and caustics are a necessary consequence of cold dark matter cosmology. It is significant in this regard that caustics of luminous matter are also believed to exist and have been observed in bright elliptical galaxies. Malin and Carter first observed ripples in the distribution of light in these galaxies [58]. Computer simulations demonstrate that when a small galaxy falls into the fixed gravitational potential of a large elliptical galaxy, the small galaxy is tidally disrupted and its stars end up on a thin ribbon in phase-space. These phase-space ribbons are like the phase-space sheets of dark matter discussed earlier, except for being limited in spatial extent. The folding of these phase-space ribbons will lead to the observed ripples in the light distribution of an elliptical galaxy which has swallowed a smaller galaxy [59, 60, 61]. There is no explanation other than the existence of caustics for the presence of these ripples in elliptical galaxies. The existence of caustics of visible matter further supports the expectation that dark matter caustics are present in galactic halos.

While virialization will thermalize the halo and destroy the oldest flows, flows will be present today from particles which have only lately fallen onto the halo. These particles will not have had sufficient time to thermalize with the rest of the halo.

Discrete flows are expected to contain a significant fraction of the local halo density, as discussed in Section 3.3. Discrete flows produce a distinct signal in an axion detector. A series of narrow peaks, one per flow, will appear in the spectra output. The width of each peak is proportional to the velocity dispersion of the corresponding flow. The power in each peak is directly proportional to the density of axions in the flow. Such narrow peaks have higher signal-to-noise ratio in a high resolution axion search. Thus, if a significant fraction of the local halo density consists of axions in such flows, a high resolution axion search increases the experiment sensitivity to axions. Furthermore, if a signal is found, it will provide detailed information on the structure of axion dark matter within our galaxy.

CHAPTER 4 HIGH RESOLUTION SEARCH FOR DARK MATTER AXIONS

4.1 Introduction

ADMX uses a microwave cavity detector to search for axions in our galactic halo [33, 62, 63, 64, 65, 66]. In its present search mode, the ADMX detector spends approximately 50 seconds at each cavity setting. As a result it can look for features in the axion frequency spectrum with a resolution of order 20 mHz. This potential has recently been realized by building the HR channel, which became fully operational in August 2002. It offers the opportunity to improve the sensitivity of the experiment by searching for the spectral features expected from the presence of discrete flows of dark matter axions. It has been demonstrated that the HR channel increases ADMX's sensitivity to an axion signal by a factor of three [35].

ADMX can operate its two channels simultaneously. The MR channel searches for broad signals, with width of order 1 kHz and a Maxwell-Boltzmann energy distribution. The HR channel searches for narrow signals arising from discrete axion flows. Each discrete flow produces a peak in the axion signal. The frequency at which a peak occurs is indicative of the square of the velocity of the corresponding flow in the laboratory frame. In searching for cold flows of axions, it is assumed that the flows are steady, i.e., the rates of change of velocity, velocity dispersion and flow density are slow compared to the time scale of the experiment. The assumption of a steady flow implies that the signal we are searching for is always present. Even so, the signal frequency will change over time due to the Earth's rotation and orbital motion [67, 68]. In addition to a signal frequency shift in data taken at different times, apparent broadening of the signal occurs because its

frequency shifts while the data are being taken. The HR channel has a frequency resolution of 0.019 Hz. To conduct a search without making assumptions about flow velocity dispersions, searches are conducted for peak power spread across several bins. We refer to the associated sum of power across n single bins as n -bin searches. These searches are performed for $n = 1, 2, 4, 8, 64, 512$ and 4096.

This chapter is on ADMX's HR channel search [69]. The experiment is described in Section 4.2. In Section 4.3, the signal expected from a microwave cavity detector observing a cold flow of axions is discussed. The detector noise characteristics are analyzed in Section 4.4. Section 4.5 contains details of the systematic corrections performed on the data. The complete analysis and axion signal search procedure are in Section 4.6. The HR search has covered the axion mass range 1.98–2.17 μeV . No axion signal was found in this range. Exclusion limits on the density of axions in local discrete flows, based on this result, are presented in Section 4.7. A discussion of the results is in Section 4.8.

4.2 Axion Dark Matter eXperiment

The microwave cavity detector utilizes the axion-electromagnetic coupling to induce resonant conversion of axions to photons. The relevant interaction is

$$\mathcal{L}_{a\gamma\gamma} = g_{a\gamma\gamma} a \mathbf{E} \cdot \mathbf{B} , \quad (4-1)$$

where a is the axion field, \mathbf{E} and \mathbf{B} are the electric and magnetic fields, respectively, and $g_{a\gamma\gamma}$ the axion-electromagnetic field coupling. The coupling depends on the fine structure constant, α , the axion decay constant, f_a , and a model dependent factor, g_γ :

$$g_{a\gamma\gamma} = \frac{\alpha g_\gamma}{\pi f_a} . \quad (4-2)$$

In the KSVZ model, $g_\gamma = -0.97$, whereas in the DFSZ model, $g_\gamma = 0.36$. The axion decay constant is related to its mass by

$$m_a = 6 \times 10^{-6} \left(\frac{10^{12} \text{GeV}}{f_a} \right) \text{eV}. \quad (4-3)$$

This coupling allows resonant conversion of axions to photons to be induced in a microwave cavity permeated by a strong magnetic field [36].

As axions in the galactic halo are non-relativistic, the energy of any single axion with velocity, v , is

$$E_a = m_a c^2 + \frac{1}{2} m_a v^2. \quad (4-4)$$

The axion-to-photon conversion process conserves energy, i.e., an axion of energy, E_a , converts to a photon of frequency, $\nu = E_a/h$. When ν falls within the bandwidth of a cavity mode, the conversion process is resonantly enhanced. The signal is a peak in the frequency spectrum of the voltage output of the detector.

The power developed in the cavity due to resonant axion-photon conversion is [36]

$$P = g_{a\gamma\gamma}^2 \frac{V B_0^2 \rho_a C}{m_a} \min(Q, Q_a), \quad (4-5)$$

where V is the cavity volume, B_0 is the magnetic field strength, ρ_a is the density of galactic halo axions at the location of the detector, Q_a is the ratio of the energy of the halo axions to their energy spread, equivalent to a “quality factor” for the halo axion signal, and C is a mode dependent form factor which is largest in the fundamental transverse magnetic mode, TM_{010} . C is given by

$$C = \frac{|\int_V d^3x \mathbf{E}_\omega \cdot \mathbf{B}_0|^2}{B_0^2 V \int_V d^3x \epsilon |\mathbf{E}_\omega|^2}, \quad (4-6)$$

in which $\mathbf{E}_\omega(\mathbf{x})e^{i\omega t}$ is the time dependent electric field of the mode under consideration, $\mathbf{B}_0(\mathbf{x})$ is the static magnetic field in the cavity and ϵ is the dielectric constant of the medium inside the cavity. The frequency-dependent form factor is evaluated

numerically. Eq. (4-5) can be recast in the convenient form,

$$P = 0.5 \times 10^{-21} \text{ W} \left(\frac{V}{500 \text{ L}} \right) \left(\frac{B_0}{7 \text{ T}} \right)^2 C \left(\frac{g_\gamma}{0.36} \right)^2 \left(\frac{\rho_a}{0.5 \times 10^{-24} \text{ g.cm}^{-3}} \right) \times \left(\frac{\nu}{1 \text{ GHz}} \right) \left(\frac{\min(Q, Q_a)}{10^5} \right). \quad (4-7)$$

A schematic of ADMX, showing both the MR and HR channels, is given in Fig. 4-1. A more detailed illustration of the magnet, cavity and cryogenic components is shown in Fig. 4-2. The microwave cavity has an inner volume, V , of 189 L. The frequency of the TM_{010} mode can be tuned by moving a pair of rods inside. The rods may be metal or dielectric and can be replaced as necessary to reach the desired frequency range. The cavity is located in the bore of a superconducting solenoid, which generates a magnetic field, B_0 , of 7.8 T. The voltage developed across a probe coupled to the electromagnetic field inside the cavity is passed to the receiver chain. As the experiment operates with the cavity at critical coupling, half the power developed in the cavity is lost to its walls and only half is passed to the receiver chain. During operation, the quality factor of the cavity, Q , is approximately 7×10^4 and the total noise temperature for the experiment, T_n , is conservatively estimated to be 3.7 K, including contributions from both the cavity and the receiver chain.

The first segment of the receiver chain is common to both the MR and HR channels. It consists of a cryogenic GaAs HFET amplifier built by NRAO, a crystal bandpass filter and mixers. At the end of this segment, the signal is centered at 35 kHz, with a 50 kHz span. The MR signal is sampled directly after this part of the receiver chain. The HR channel contains an additional bandpass filter and mixer, resulting in a spectrum centered at 5 kHz with a 6 kHz span.

Time traces of the voltage output from the receiver, consisting of 2^{20} data points, are taken with sampling frequency 20 kHz in the HR channel. This results in a data stream of 52.4 s in length, corresponding to 0.019 Hz resolution in the

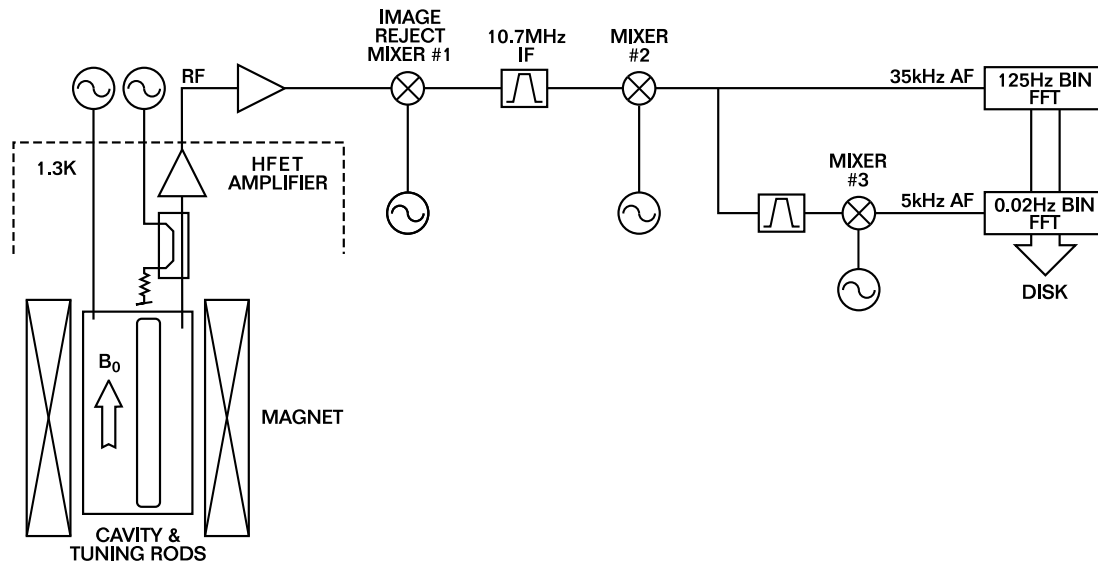


Figure 4-1. Schematic diagram of the receiver chain.

frequency spectrum. The data were primarily taken in parallel with the operations of the MR channel over a period beginning in November, 2002 and ending May, 2004. Continuous HR coverage has been obtained and candidate peak elimination performed for the frequency range 478–525 MHz, corresponding to the axion mass range 1.98–2.17 μeV . Data with Q less than 40 000 and/or cavity temperature above 5 K were discarded. When this was the case, additional data were taken to ensure coverage of the full range.

4.3 Axion Signal Properties

The HR channel is used to search for narrow peaks caused by flows of cold axions through the detector. It is assumed that the flows are steady, i.e., the rates of change of velocity, velocity dispersion and density of these flows are slow compared to the time scale of the experiment. The assumption of a steady flow implies that the signal we are searching for is always present. Even so, the kinetic energy term in Eq. (4-4) and the corresponding frequency change over time due to the Earth’s rotational and orbital motions. In addition to a signal frequency shift

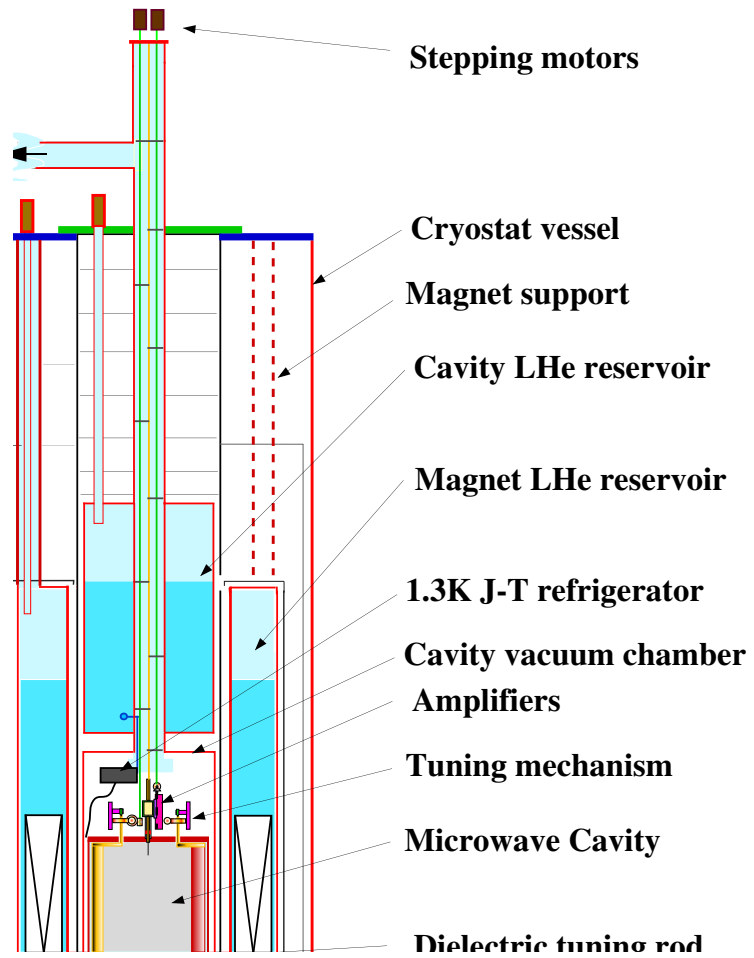


Figure 4-2. Sketch of the ADMX detector.

in data taken at different times, apparent broadening of the signal occurs because its frequency shifts while the data are being taken.

Using Eq. 4-4, one sees that ratio of the shift in frequency, Δf , to the base frequency, f , due to a change in velocity, Δv , is

$$\frac{\Delta f}{f} = \frac{m_a v \Delta v}{m_a c^2 + \frac{1}{2} m_a v^2} \quad (4-8)$$

$$\implies \Delta f = \frac{f v \Delta v}{c^2} . \quad (4-9)$$

The velocity of a dark matter flow relative to the Earth will be in the range 100 – 1000 km/s. We chose $v = 600$ km/s as a representative value for the purpose of estimation. A frequency of $f = 500$ MHz is chosen as typical for the data under consideration.

The magnitude of the velocity on the surface of Earth at the equator due to the Earth's rotation is $v_R = 0.4$ km/s. It is less than this at the location of the axion detector, but this value is used for the purpose of illustration. Assuming the extreme case of alignment of the Earth's rotational velocity with the flow velocity, $\Delta v = 2v_R$. The resulting daily signal modulation is 3 Hz. Approximating the Earth's orbit as circular, the magnitude of it's velocity with respect to the Sun is $v_T = 30$ km/s. Again, considering the extreme case of velocity alignment, the frequency modulation due to the orbit of Earth around the Sun is at most 200 Hz.

The bandwidth of the HR channel is 6 kHz. After identifying candidate frequencies, they are reexamined to see if they satisfy the criterion of a constantly present signal. Thus, if the spectrum is centered on the candidate frequency when it is reexamined, the signal will still be within the detector bandwidth as it will move at most 200 Hz from its original frequency.

In addition, both the rotation of the Earth and its motion around the Sun will result in a small change in the flow velocity relative to the detector while

each spectrum is taken and a subsequent increase in the signal line-width relative to what would be expected in the static case. Similarly to Eq. (4-9), the signal broadening, δf , due to a change in the flow velocity, δv , is

$$\delta f = \frac{fv\delta v}{c^2} . \quad (4-10)$$

Taking the time of integration to be $\Delta t \simeq 50$ s, the change in relative velocity is at most

$$\delta v = 2\pi v_m \left(\frac{\Delta t}{T} \right) \quad (4-11)$$

where T is the period of the motion (diurnal or annual) and v_m is the respective velocity (v_R or v_T). The line-width is increased by 4×10^{-3} Hz due to the Earth's rotation. The Earth's orbital motion increases the line-width by 10^{-3} Hz. The spectral resolution of the HR channel is 0.019 Hz, large enough to make these effects negligible.

For flows of negligible velocity dispersion, the sensitivity of the experiment is proportional to the frequency, f , and the time of integration, Δt , provided the resolution, $B = 1/\Delta t$, is less than the shift of the signal frequency during measurement. This requirement allows a measurement integration time as long as

$$\delta t < 160 \text{ s} \left(\frac{500 \text{ MHz}}{f} \right)^{\frac{1}{2}} . \quad (4-12)$$

This suggests that for the data this note is based on, a more sensitive limit could have been achieved with a longer integration time than the actual 52 s.

The velocity dispersion of the flow may, however, be a limiting factor. While no value for velocity dispersion is assumed in performing the HR analysis, for illustrative purposes, let us consider a particular case: the ‘‘Big Flow,’’ discussed by Sikivie [45]. The upper bound on the velocity dispersion of this flow is $\delta v \lesssim 50$ m/s. This leads to a maximum line broadening of $\delta f_{BF} \lesssim 8 \times 10^{-2}$ Hz, i.e., a signal from axions in the Big Flow is spread over four frequency bins in the

detector spectrum if the limit $\delta v \lesssim 50$ m/s is saturated. Let us emphasize, however, that there is no reason to believe this bound is saturated.

In general, we do not know the velocity dispersion of the cold axion flows for which we search. Subsequently, we do not know the signal width. To compensate, searches are performed at multiple resolutions by combining 0.019 Hz wide bins. These searches are referred to as n -bin searches, where $n = 1, 2, 4, 8, 64, 512$ and 4096. For $f = 500$ MHz and $v = 600$ km/s, the corresponding flow velocity dispersions are

$$\delta v_n = 6 n \text{ m/s} \left(\frac{600 \text{ km/s}}{v} \right). \quad (4-13)$$

Further details of the n -bin searches are given in Section 4.6.

4.4 Noise Properties

The power output from the HR channel is expressed in units of σ , the rms noise power. This noise power is related to the noise temperature, T_n , via

$$\sigma = k_B T_n \sqrt{\frac{b}{\Delta t}}, \quad (4-14)$$

where k_B is Boltzmann's constant and b is the frequency resolution. The total noise temperature, $T_n = T_C + T_{el}$, where T_C is the physical cavity temperature and T_{el} is the electronic noise contribution from the receiver chain. As no averaging is performed in HR sampling, $b = 1/\Delta t$. Thus, the rms noise power is

$$\sigma = k_B b T_n. \quad (4-15)$$

Output power is normalized to σ and T_n is used to determine this power. Eq. (4-15) has been verified experimentally by allowing the cavity to warm and observing that σ is proportional to T_C .

The noise in the HR channel has an exponential distribution. The noise in a 1-bin is the sum of independent sine and cosine components, as no averaging is performed in HR sampling. The energy distribution should be proportional to a

Boltzmann factor, $\exp(-E/kT)$, and non-relativistic and classical energies, such as $E = (1/2)mv^2$ or $E = (1/2)kx^2$, are proportional to squares of the amplitude. Thus, the noise amplitude, a , for a single component (i.e., sine or cosine) has a Gaussian probability distribution,

$$\frac{dP}{da} = \frac{1}{\sqrt{2\pi}\sigma_a} \exp\left(-\frac{a^2}{2\sigma_a^2}\right), \quad (4-16)$$

where σ_a is the standard deviation.

As there are two components per bin, the addition of n bins is that of $2n$ independent contributions. The probability distribution, dP/dp_n , of observing noise power p_n in an n -bin is

$$\frac{dP}{dp_n} = \left(\prod_{i=1}^{2n} \int_{-\infty}^{\infty} da_i \right) \frac{\exp\left(-\frac{1}{2\sigma_a^2} \sum_{j=1}^{2n} a_j^2\right)}{(\sqrt{2\pi}\sigma_a)^{2n}} \delta\left(p_n - \sum_{k=1}^{2n} \frac{a_k^2}{2}\right). \quad (4-17)$$

Evaluating the above expression,

$$\frac{dP}{dp_n} = \frac{p_n^{n-1}}{(n-1)!\sigma_a^{2n}} \exp\left(-\frac{p_n}{\sigma_a^2}\right). \quad (4-18)$$

For $n = 1$,

$$\frac{dP}{dp_1} = \frac{1}{\sigma_a^2} \exp\left(-\frac{p_1}{\sigma_a^2}\right), \quad (4-19)$$

which is indeed a simple exponential, as expected.

Using this noise distribution, we can easily see that the average (rms) noise power in the one bin search is $\sigma = \sigma_a^2$. Substituting this in (4-19), the noise power distribution function becomes

$$\frac{dP}{dp_1} = \frac{1}{\sigma} \exp\left(-\frac{p_1}{\sigma}\right). \quad (4-20)$$

For each HR spectrum, σ is determined by plotting the number of frequency bins, N_p , with power between p and $p + \Delta p$ against p . According to Eq. (4-20),

$$N_p = \frac{N\Delta p}{\sigma} e^{-\frac{p}{\sigma}}, \quad (4-21)$$

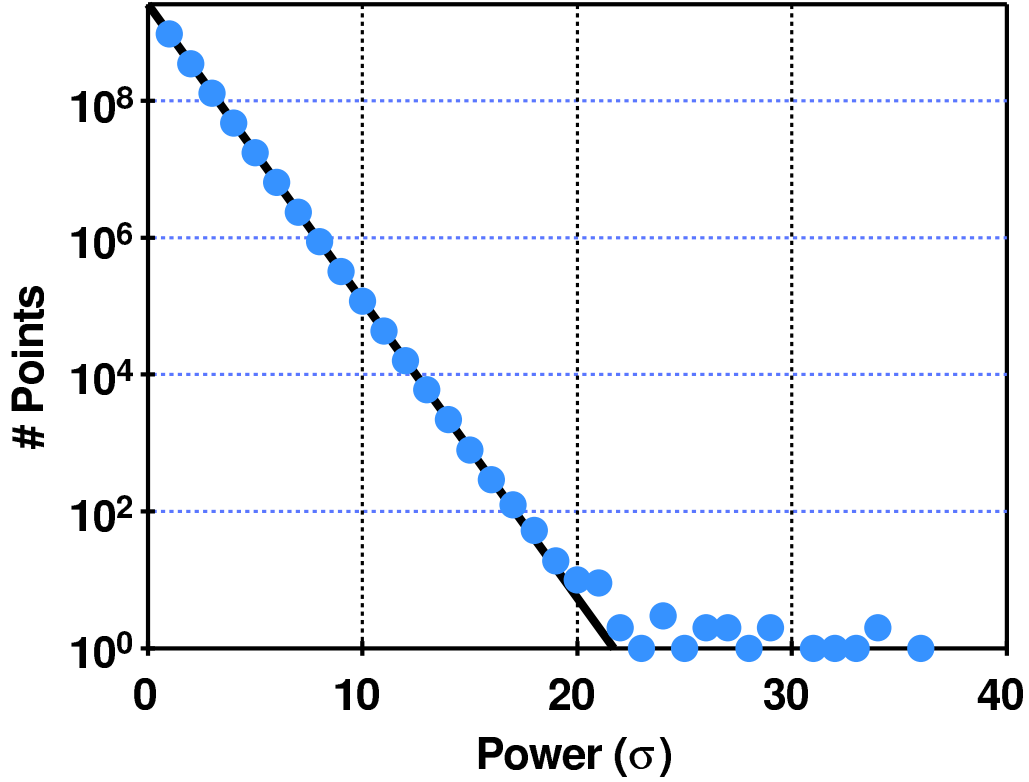


Figure 4-3. Power distribution for a large sample of 1-bin data.

where N is the total number of frequencies. As

$$\ln N_p = -\frac{p}{\sigma} + \ln \left(\frac{N \Delta p}{\sigma} \right), \quad (4-22)$$

σ is the inverse of the slope of the $\ln N_p$ versus p plot. Figure 4-3 demonstrates that the data is in good agreement with this relation for p less than 20σ . The deviation of the data from Eq. (4-22) for p greater than 20σ is due to the fact that the background is not pure noise, but also contains environmental signals of a non-statistical nature.

As we combine an increasing number of bins, the noise power probability distribution approaches a Gaussian, in accordance with the central limit theorem. The right-hand side of Eq. (4-18) approaches a Gaussian in the limit of large n . We have examined a large sample of noise in each n -bin search and verified that it is distributed according to Eq. (4-18). Figures 4-4 through 4-9 show the

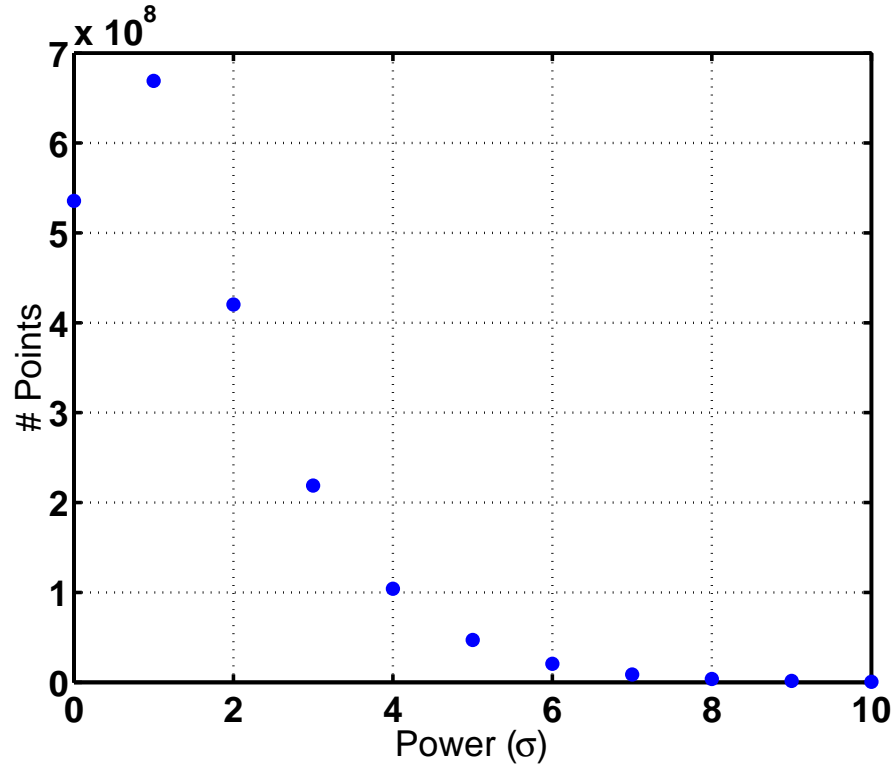


Figure 4-4. Power distribution for a large sample of 2-bin data.

progression from the exponential distribution of Fig. 4-3 to a near Gaussian curve for the 4096-bin search.

In addition to examining the behavior of the noise statistics, we have performed a cross-calibration between the HR and MR channels. The signal power of an environmental peak, observed at 480 MHz and shown in Fig. 4-10, was examined in both the HR and MR channels. The observed HR signal power was $(1.8 \pm 0.1) \times 10^{-22}$ W, where the error quoted is the statistical uncertainty. The MR channel observed signal power 1.7×10^{-22} W, in agreement with the HR channel. Note that the MR signal was acquired with a much longer integration time than that of the HR signal (2000 s for MR versus 52 s for HR).

The combination of the calibration of the noise power with cavity temperature, the consistency between expected and observed noise statistics and the agreement

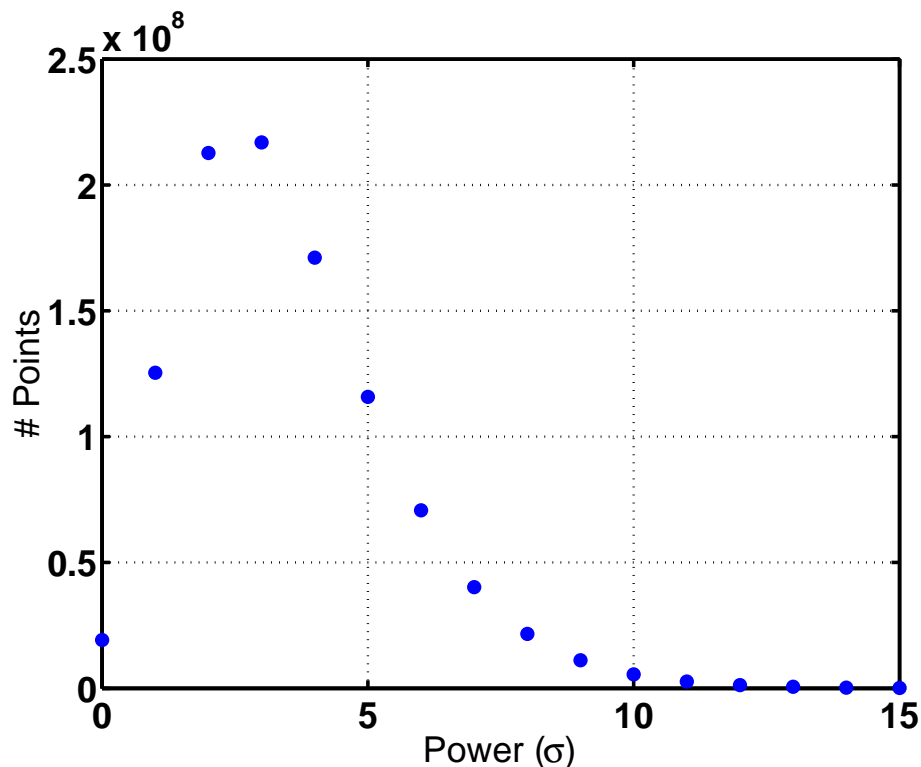


Figure 4-5. Power distribution for a large sample of 4-bin data.

of signal power observed in both the HR and MR channels, makes us confident that the signal power is accurately determined in the HR channel.

4.5 Removal of Systematic Effects

There are two systematic effects introduced in the receiver chain shown in Fig. 4-1. Two passband filters are present on the HR receiver chain: one with bandwidth 35 kHz on the shared MR-HR section and a passive LC filter of bandwidth 6 kHz, seen by the HR channel only. The combined response of both these filters has been analyzed and removed from the data. The second systematic effect is due to the frequency-dependent response of the coupling between the cavity and the first cryogenic amplifier. This effect is removed using the equivalent circuit model described later.

The combined passband filter response was determined by taking data with a white noise source at the rf input of the receiver chain. A total of 872 time traces

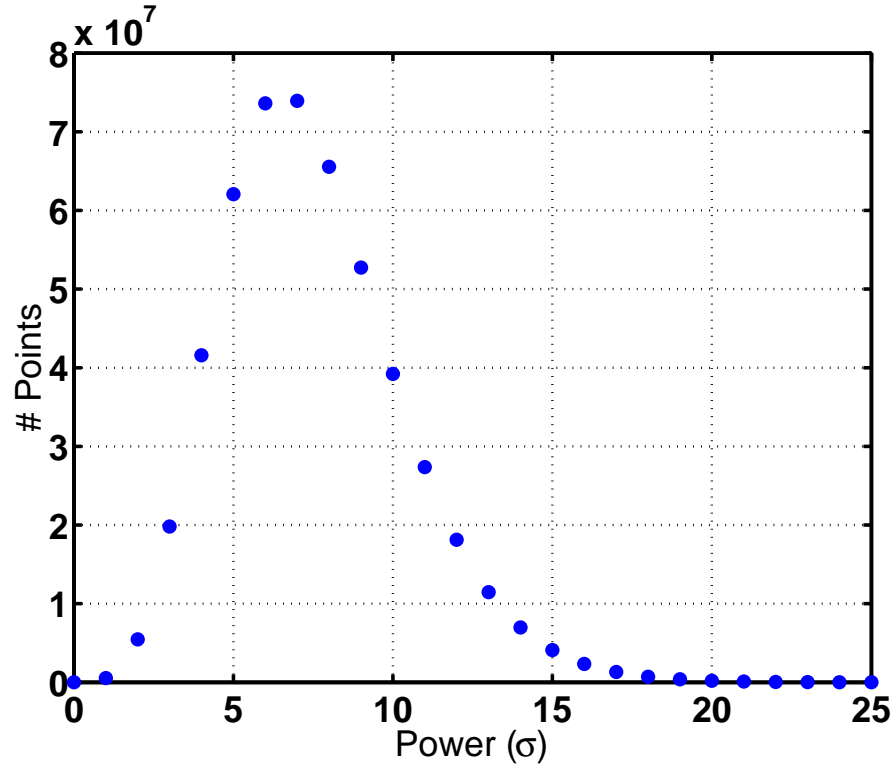


Figure 4-6. Power distribution for a large sample of 8-bin data.

were recorded over a two day period. In order to achieve a reasonably smooth calibration curve, 512 bins in the frequency spectrum for each time trace were averaged giving 9.77 Hz resolution. The combined average of all data is shown in Fig. 4-11. This measured response was removed from all data used in the HR search, as follows. The raw power spectra have frequency 0–10 kHz, where the center frequency of 5 kHz has been mixed down from the cavity frequency. Each raw power spectrum is cropped to the region 2–8 kHz to remove the frequencies not within the LC filter bandwidth. Each remaining frequency bin is then weighted by a factor equal to the receiver chain response at the given frequency divided by the maximum receiver chain response. Interpolation for frequency points not specifically included in the calibration curve is performed by assuming that each point on the calibration curve was representative of 512 bins centered on that frequency, so all power corresponding to frequencies within that range is normalized

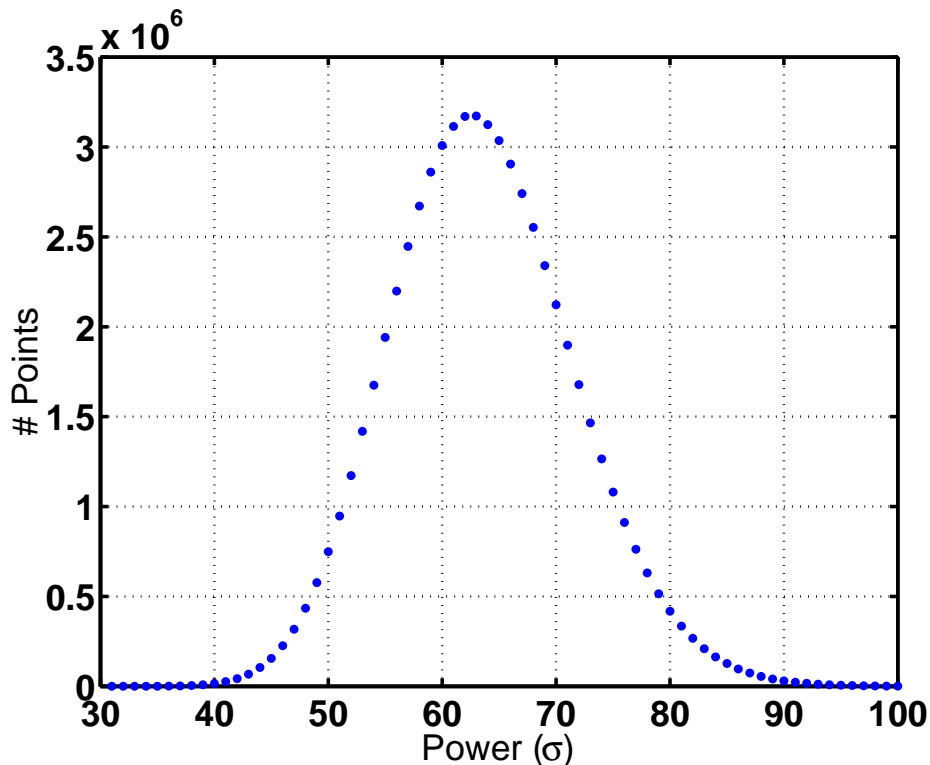


Figure 4–7. Power distribution for a large sample of 64-bin data.

by the same factor. As the calibration curve varies slowly with frequency within the window to which each spectra is cropped, this is an adequate treatment of the normalization.

In the MR channel, the effect of the cavity-amplifier coupling is described using an equivalent-circuit model [70]. This model has been adapted for use in the HR channel. The frequency dependent response of the cavity amplifier coupling is most evident in the 4096-bin search, thus this is the data used to apply the equivalent circuit model. A sample spectrum before correction is shown in Fig. 4–12.

In the equivalent-circuit model, each frequency is given by Δ , the number of bins it is offset from the bin of the center frequency, measured in units of the 4096-bin resolution, i.e. $b_{4096} = 78.1$ Hz. The equivalent-circuit model predicts that the power (in units of the rms noise) at the NRAO amplifier output (the point

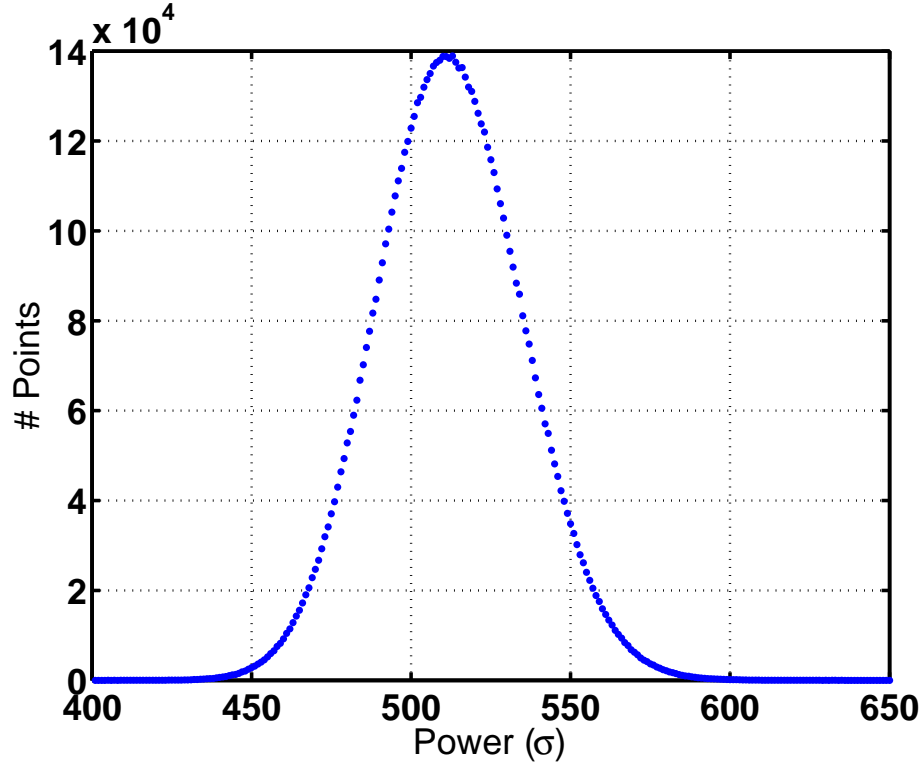


Figure 4–8. Power distribution for a large sample of 512-bin data.

labelled “RF” in Fig. 4–1) in the 4096–bin search at the frequency offset Δ is

$$P(\Delta) = \frac{a_1 + 8a_3 \left(\frac{\Delta - a_5}{a_2}\right)^2 + 4a_4 \left(\frac{\Delta - a_5}{a_2}\right)}{1 + 4 \left(\frac{\Delta - a_5}{a_2}\right)^2}, \quad (4-23)$$

where the parameters a_1 through a_5 are

$$a_1 = (b_{4096}/b)(T_C + T_I + T_V)/T_n, \quad (4-24)$$

$$a_2 = f_0/(b_{4096} Q), \quad (4-25)$$

$$a_3 = (b_{4096}/b)(T_I + T_V + (T_I - T_V) \cos(2kL))/T_n, \quad (4-26)$$

$$a_4 = (b_{4096}/b)((T_I - T_V) \sin(2kL))/T_n \text{ and} \quad (4-27)$$

$$a_5 = (f_0 - f_{cen})/b_{4096}. \quad (4-28)$$

In the above expressions, T_C is the physical temperature of the microwave cavity, T_I and T_V are the current and voltage noise, respectively, contributed by the

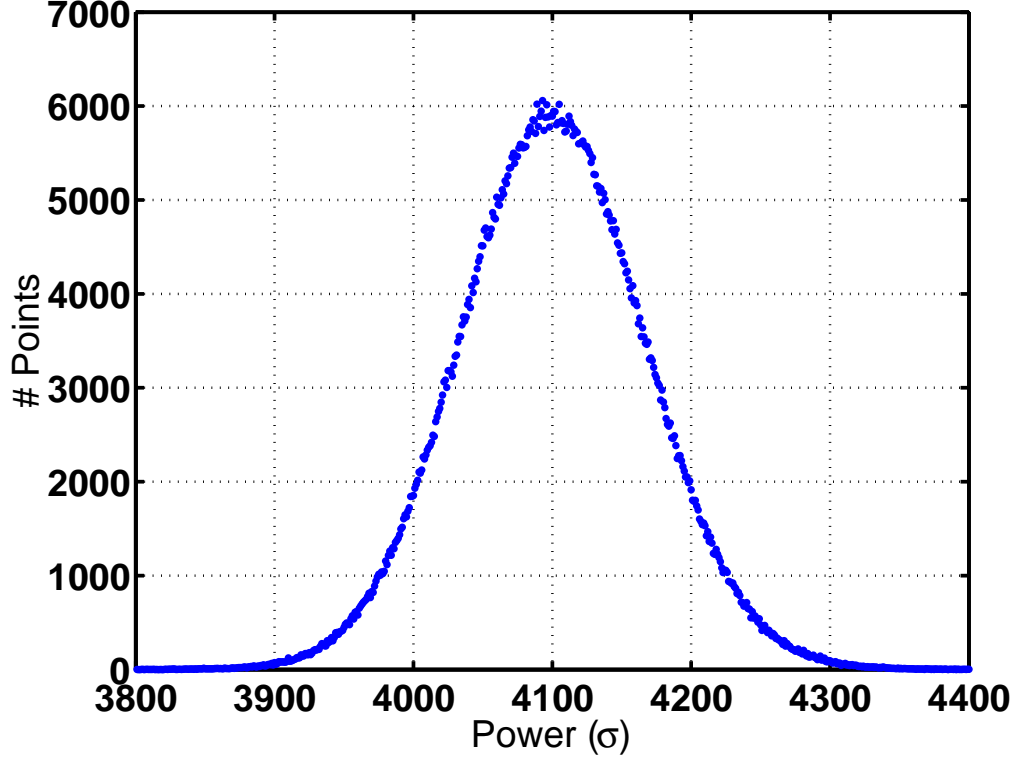


Figure 4-9. Power distribution for a large sample of 4096-bin data.

amplifier, T_n is the noise temperature contributed from all components, b is the frequency resolution of the HR channel, i.e. 0.019 Hz, L is the electrical (cable) length from the cavity to the HFET amplifier, f_0 is the cavity resonant frequency, f_{cen} is the center frequency of the spectrum and k is the wavenumber corresponding to frequency $f_{cen} + b\Delta$. The factor b_{4096}/b appears in the parameters a_1 , a_3 and a_4 as it is an overall factor which results from normalizing the power to the single bin noise baseline. In practice, the parameters a_1 through a_5 are established by fitting. The line in Fig. 4-12 shows the fit obtained using the equivalent circuit model.

Large peaks in the data, e.g. an axion signal or environmental peak, are removed before fitting to prevent bias. The 4096-bin spectrum is used to perform the fit and then the original 1-bin spectrum is corrected to remove the systematic effect. The weighting factors are calculated using Eq. (4-23) and the fitted parameters, a_1 through a_5 , at the center of each bin of width b_{4096} . These factors are

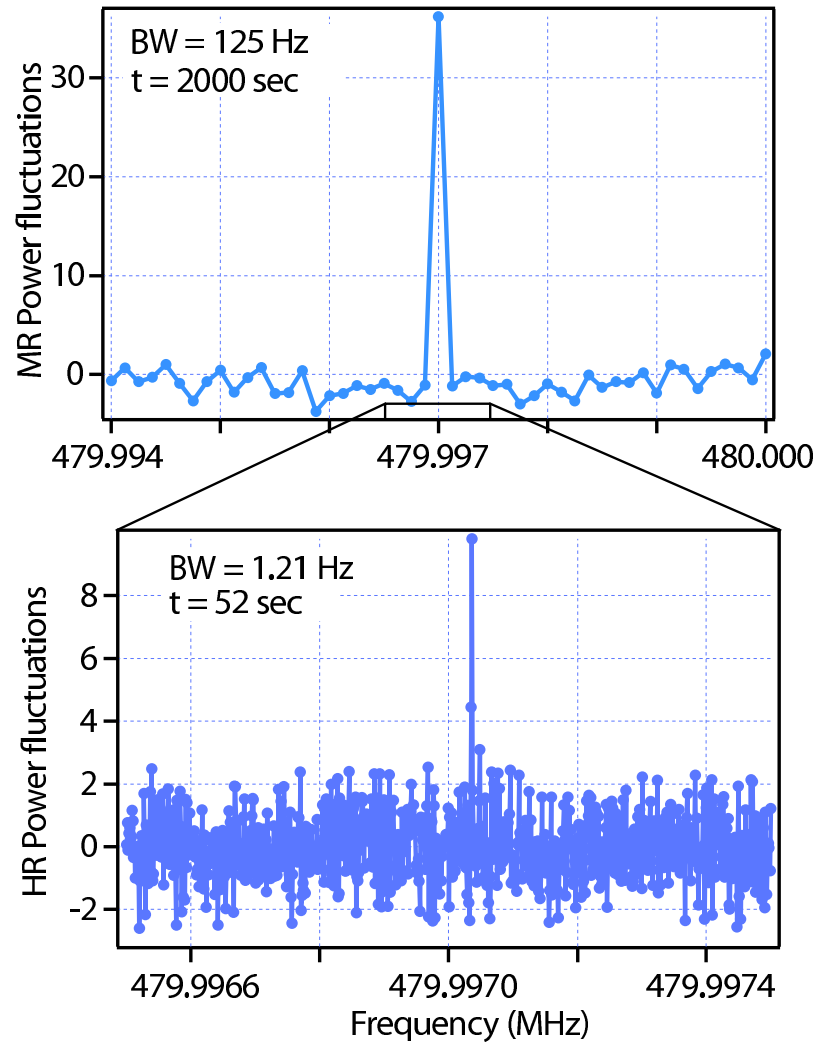


Figure 4–10. An environmental peak as it appears in the MR search (top) and the 64-bin HR search. The unit for the vertical axis is the rms power fluctuation in each case.

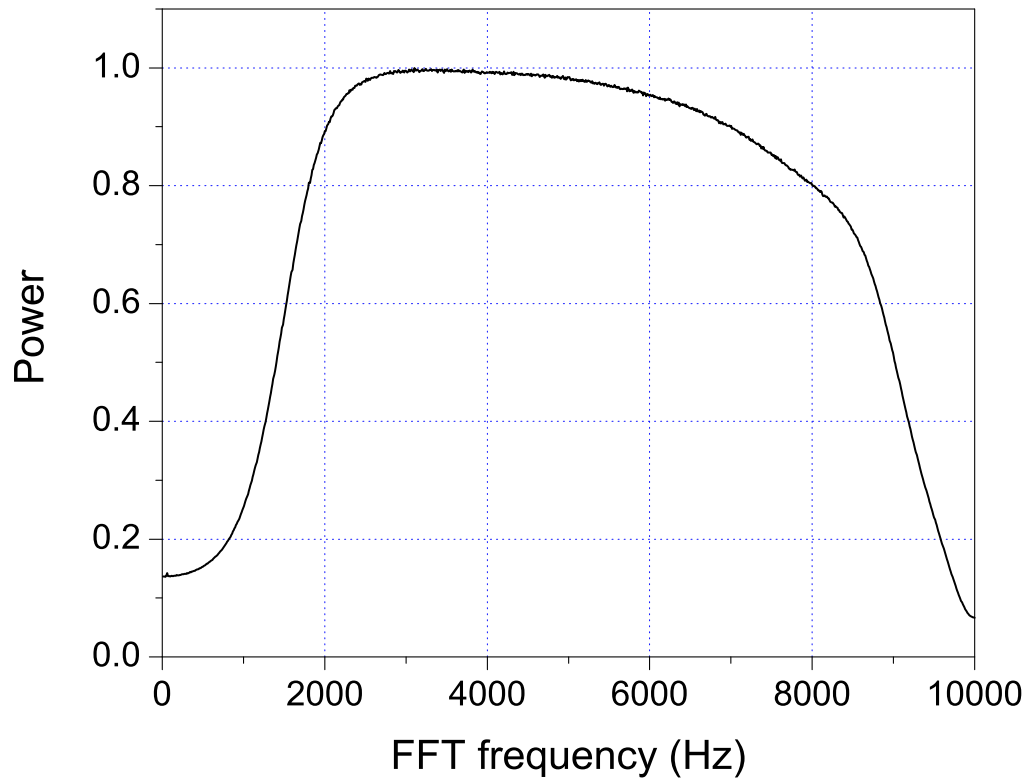


Figure 4–11. HR filter response calibration data (512 bin average). The power has been normalized to the maximum power output.

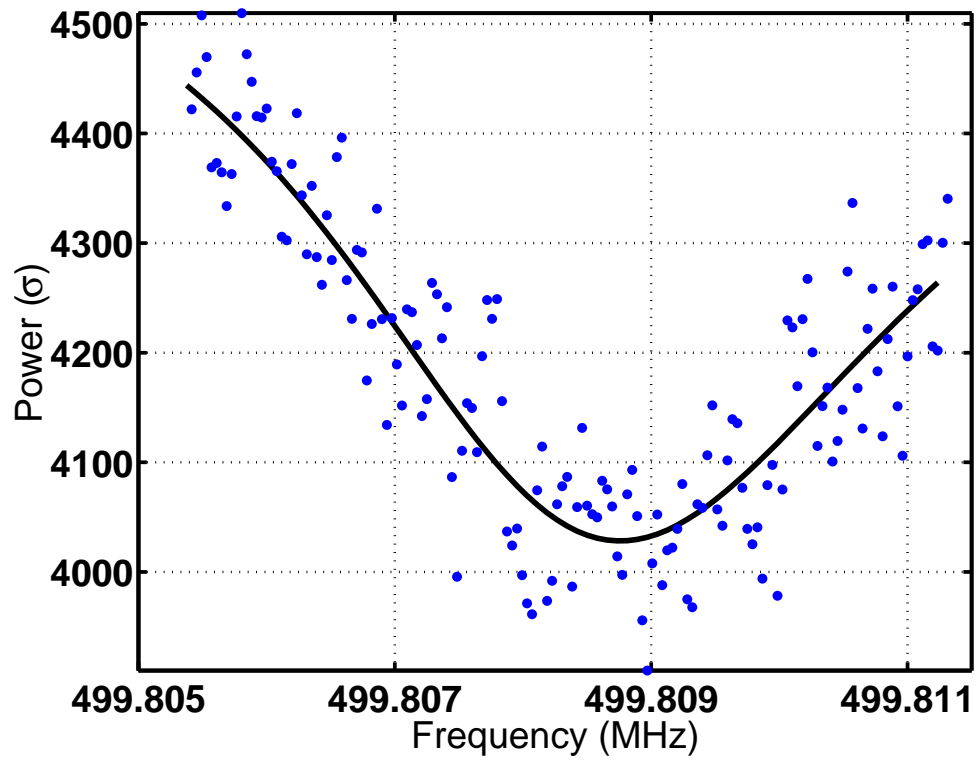


Figure 4–12. Sample 4096-bin spectrum before correction for the cavity-amplifier coupling. The line is the fit obtained using the equivalent circuit model.

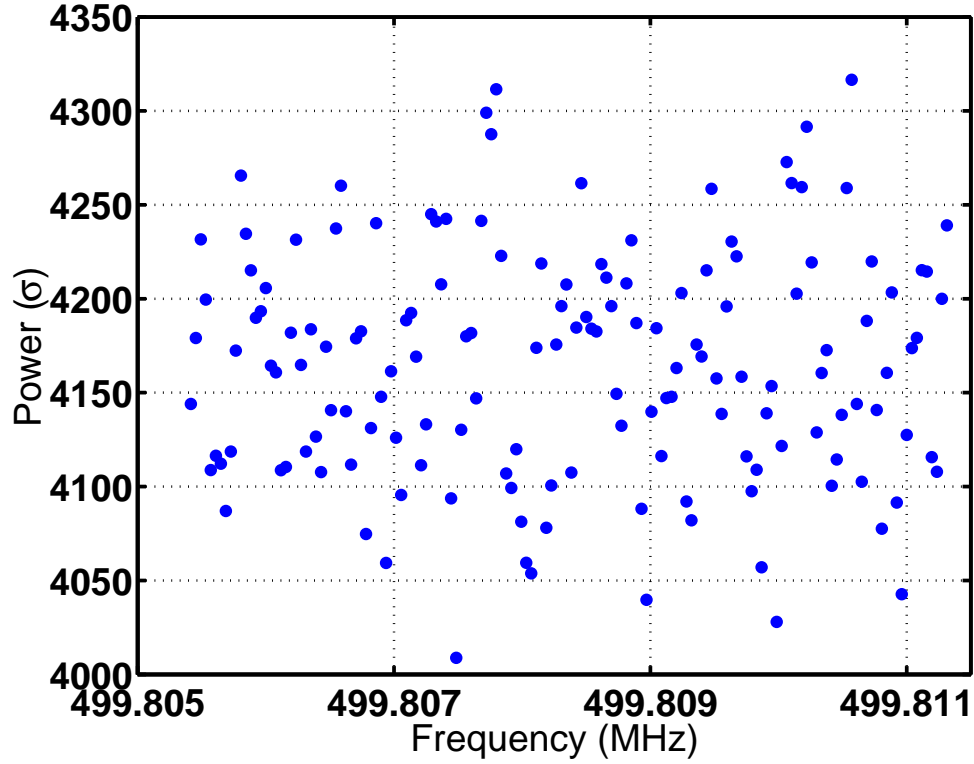


Figure 4–13. The same 4096-bin spectrum of Fig. 4–12 after correction for the cavity-amplifier coupling.

the ratio of the fit at a given point to the maximum value of the fit. Each 1-bin is multiplied by the factor calculated for the bin of width b_{4096} within which it falls.

Figure 4–13 shows the spectrum of Fig. 4–12 after removal of systematic effects. The removal of the cavity-amplifier coupling and the passband filter response using the techniques described above results in flat HR spectra.

4.6 Axion Signal Search

We now describe the search for an axion signal and summarize the analysis performed on each time trace.

The width of an axion signal is determined by the signal frequency, axion velocity and flow velocity dispersion (Eq. (4–10)), the latter being the most uncertain variable. n -bin searches, where n is the number of adjacent 1-bins added together ($n = 1, 2, 4, 8, 64, 512$ and 4096), are conducted to allow for various

1-bin search:	1	2	3	4	5	6	7	8	9	10	11	12	13	14	15	16
2-bin search:	1 2		3 4		5 6		7 8		9 10		11 12		13 14		15 16	
	2 3		4 5		6 7		8 9		10 11		12 13		14 15			
4-bin search:	1 2 3 4				5 6 7 8				9 10 11 12				13 14 15 16			
	3 4 5 6				7 8 9 10				11 12 13 14							
8-bin search:	1 2 3 4 5 6 7 8								9 10 11 12 13 14 15 16							
	5 6 7 8 9 10 11 12															

Figure 4–14. Illustration of the addition scheme for the 2, 4 and 8-bin searches. The numbers correspond to the data points of the 1-bin search. Numbers within the same box are bins added together to form a single datum in the n -bin searches with $n > 1$.

velocity dispersions. For searches with $n > 1$, there is an overlap between successive n -bins such that each n -bin overlaps with the last half of the previous and first half of the following n -bin. This scheme is illustrated for the 2, 4 and 8-bin searches in Fig. 4–14.

The search for an axion signal is performed by scanning each spectrum for peaks above a certain threshold. All such peaks are considered candidate axion signals. The thresholds are set at a level where there is only a small probability that a pure noise peak will occur and such that the number of frequencies considered as candidate axion peaks is manageable. The candidate thresholds used were 20, 25, 30, 40, 120, 650 and 4500 σ , in increasing order of n .

All time traces are analyzed in the same manner. A fast Fourier transform is performed and an initial estimate of σ is obtained by fitting the 1-bin noise distribution to Eq. (4–22). Systematic effects are then removed, i.e. the corrections described in Section 4.5 for the filter passband response and cavity–amplifier coupling are performed. “Large” peaks not included in the equivalent circuit model fit for the cavity-amplifier response are defined to be those greater than 120% of the search threshold for each n -bin search. After the removal of systematic effects, the 1-bin noise distribution is again fitted to Eq. (4–22) to obtain the true value of σ and the search for peaks above the thresholds takes place.

The axion mass is not known, requiring that a range of frequencies must be examined. Full HR coverage has been obtained for the region 478–525 MHz, corresponding to axion masses between 1.98 and 2.17 μeV . The selected frequency range is examined in three stages for axion peaks, as follows:

Stage 1: Data for the entire selected frequency range is taken. The frequency step between successive spectra is approximately 1 kHz, i.e. the center frequency of each spectrum differs from the previous spectrum by 1 kHz. Frequencies at which candidate axion peaks occur are recorded for further examination during stage 2.

Stage 2: Multiple time traces are taken at each candidate frequency from stage 1. The steady flow assumption means that a peak will appear in spectra taken with center frequency equal to the candidate frequency from stage 1 if such a peak is an axion signal. The frequencies of persistent peaks, i.e. peaks that appear during both stage 1 and 2 are examined further in stage 3.

Stage 3: Frequencies of persistent peaks undergo a three-part examination. The first step is to repeat stage 2, to ensure the peaks still persist. Secondly, the warm port attenuator is removed from the cavity and multiple time traces taken. If the peak is due to external radio signals entering the cavity (an environmental peak), the signal power will increase dramatically. If the signal originates in the cavity due to axion-photon conversion, the power developed in the cavity will remain the same as that for the normal configuration. The third step is to use an external antenna probe as a further confirmation that the signal is environmental. Some difficulties were encountered with the antenna probe, due to polarization of environmental signals. However, the second step is adequate to confirm that peaks are environmental. If a persistent peak is determined to not be environmental, a final test will confirm that it is an axion signal. The power in such a signal must grow proportionally with the square of the magnetic field (B_0 in Eq. (4-7)) and disappear when the magnetic field is switched off.

No axion peaks were found in the range 478–525 MHz using this approach. The exclusion limit calculated from this data is discussed in the following section.

4.7 Results

Over the frequency range 478–525 MHz, we derive an upper limit on the density of individual flows of axion dark matter as a function of the velocity dispersion of the flow. The corresponding axion mass range is 1.97–2.17 μeV . Each n -bin search places an upper limit on the density of a flow with maximum velocity dispersion, δv_n , as given by Eq. (4–13).

Several factors reduce the power developed in an axion peak from that given in Eq. (4–7). The experiment is operated near critical coupling of the cavity to the preamplifier, so that half this power is observed when the cavity resonance frequency, f_0 , is precisely tuned to the axion energy. If f_0 is not at the center of a 1-bin, the power is spread into adjacent bins, as discussed below. When the axion energy is off-resonance, but still within the cavity bandwidth at a frequency f , the Lorentzian cavity response reduces the power developed by an additional factor of

$$h(f) = \frac{1}{1 + 4Q^2 \left(\frac{f}{f_0} - 1\right)^2}. \quad (4-29)$$

To be conservative, we calculate the limits at points where successive spectra overlap, i.e. at the frequency offset from f_0 that minimizes $h(f)$.

If a narrow axion peak falls at the center of a 1-bin, all power is deposited in that 1-bin. However, if such a peak does not fall at the center of a 1-bin, the power will be spread over several 1-bins. We now calculate the minimum power in a single n -bin caused by a randomly situated, infinitely narrow axion line. The data recorded is the voltage output from the cavity as a function of time. The voltage as a function of frequency is obtained by Fourier transformation and then squared to obtain a raw “power” spectrum. The actual power is obtained by comparison to the rms noise power. The data are sampled for a finite amount of time and thus,

the Fourier transformation of the output, $\mathcal{F}(f)$, will be of the voltage multiplied by a windowing function, i.e.,

$$\mathcal{F}(f) = \int_{-\infty}^{\infty} v(t)w(t) \exp(i2\pi ft) dt , \quad (4-30)$$

where $v(t)$ is the measured output voltage and $w(t)$ is the windowing function for a sampling period T ,

$$w(t) = \begin{cases} 1 & \text{if } -T/2 \leq t \leq T/2 , \\ 0 & \text{otherwise .} \end{cases} \quad (4-31)$$

Eq. (4-30) is equivalent to

$$\mathcal{F}(f) = \int_{-\infty}^{\infty} V(k)W(f-k)dk , \quad (4-32)$$

where $V(f)$ and $W(f)$ are the Fourier transforms of the output voltage, $v(t)$, and the windowing function, $w(t)$, i.e., $\mathcal{F}(f)$ is the convolution of $V(f)$ and $W(f)$, given by

$$W(f) = \frac{\sin(\pi fT)}{\pi f} . \quad (4-33)$$

Discretizing Eq. (4-32) and inserting Eq. (4-33), we have

$$\mathcal{F}(f) = \sum_{m=0}^N V((m + \frac{1}{2})b) \frac{\sin(\pi(\frac{f}{b} - (m + \frac{1}{2})))}{\pi(\frac{f}{b} - (m + \frac{1}{2}))} , \quad (4-34)$$

where b is the frequency resolution of the HR channel, $2N$ points are taken in the original time trace, and the center frequency of the j th 1-bin is $(j + 1/2)b$. Thus, for an axion signal of frequency f falling in 1-bin j , a fraction of the power,

$$g(m) = \left(\frac{\sin(m\pi + \delta)}{m\pi + \delta} \right)^2 , \quad (4-35)$$

is lost to the m th 1-bin from 1-bin j , where $\delta = \pi(m + 1/2 - f/b)$. If $\delta = 0$, i.e, the axion signal frequency is exactly equal to a 1-bin center frequency, all the power is deposited in a single 1-bin. However, if this is not the case, power is lost to other 1-bins. In setting limits, we assume that the power loss is maximal.

The maximum power loss occurs when a signal in the 1-bin search falls exactly between the center frequency of two adjacent 1-bins. In this case, when $\delta = \pi/2$, Eq. (4-35) shows that 40.5% of the power will be deposited in each of two 1-bins. In n -bin searches with $n \geq 2$, not as much power is lost to other n -bins, due to the overlap between successive n -bins. The minimum power deposited in an n -bin is 81% for $n = 2$, 87% for $n = 4$ and 93% for $n = 8$. For $n = 64, 512$ and 4096 , the amount of power not deposited in a single n -bin is negligible.

For the n -bin searches with $n = 64, 512$ and 4096 , a background noise subtraction was performed which will lead to exclusion limits at the 97.7% confidence level. These limits are derived using the power at which the sum of the signal power and background noise power have a 97.7% probability to exceed the candidate thresholds. We call this power the “effective” threshold for each search. The effective thresholds are obtained by integrating the noise probability distribution, Eq. (4-18), numerically solving for the background noise power corresponding to the 97.7% confidence level for each n and subtracting these values from the original candidate thresholds. For $n = 64, 512$ and 4096 , the effective thresholds are 71, 182 and 531 σ , respectively. For smaller values of n , background noise subtraction does not significantly improve the limits and the effective threshold was taken to be the candidate threshold. Table 4-1 summarizes this information and shows the frequency resolution of each search with the corresponding maximum flow velocity dispersion from Eq. (4-13) for $v = 600$ km/s.

Our exclusion limits were calculated for an axion signal with power above the effective threshold reduced by the appropriate factors. These factors arise from the critical coupling, the Lorentzian cavity response and the maximum power loss due to the peak not falling in the center of an n -bin, as outlined above. Equations (4-7) and (4-15) were used, for both KSVZ and DFSZ axion couplings. The cavity volume, V , is 189 L. Measured values of the quality factor, Q , the magnetic field,

n	Effective threshold (σ)	b_n (Hz)	δv_n (m/s)
1	20	0.019	6
2	25	0.038	10
4	30	0.076	20
8	40	0.15	50
64	71	1.2	400
512	182	9.8	3000
4096	531	78	20000

Table 4–1. Effective power thresholds for all n -bin searches, with the frequency resolutions, b_n and corresponding maximum flow velocity dispersions, δv_n , for a flow velocity of 600 km/s.

Frequency (MHz)	C	T_{el} (K)
450	0.43	1.9
475	0.42	1.9
500	0.41	1.9
520	0.38	1.9
550	0.36	2.0

Table 4–2. Numerically calculated values of the form factor, C , and amplifier noise temperatures, T_{el} , from NRAO specifications.

B_0 , and the cavity temperature, T_C , are recorded in each data file. Numerically determined values of the form factor, C are given in Table 4–2. The electronic noise temperature, T_{el} , was conservatively taken from the specifications of the NRAO amplifier, the dominant source of noise in the receiver chain, although our measurements indicate that T_{el} is less than specified. These values are also given in Table 4–2. Linear interpolation between values at the frequencies specified was used to obtain values of C and T_{el} at all frequencies.

The 2-bin search density exclusion limit obtained using these values is shown in Fig. 4–15. For values of n other than $n = 2$, the exclusion limits differ by only constant factors. The constant factors are 1.60, 1.00, 1.12, 1.39, 2.53, 5.90 and 17.2 for $n = 1, 2, 4, 8, 64, 512$ and 4096, respectively.

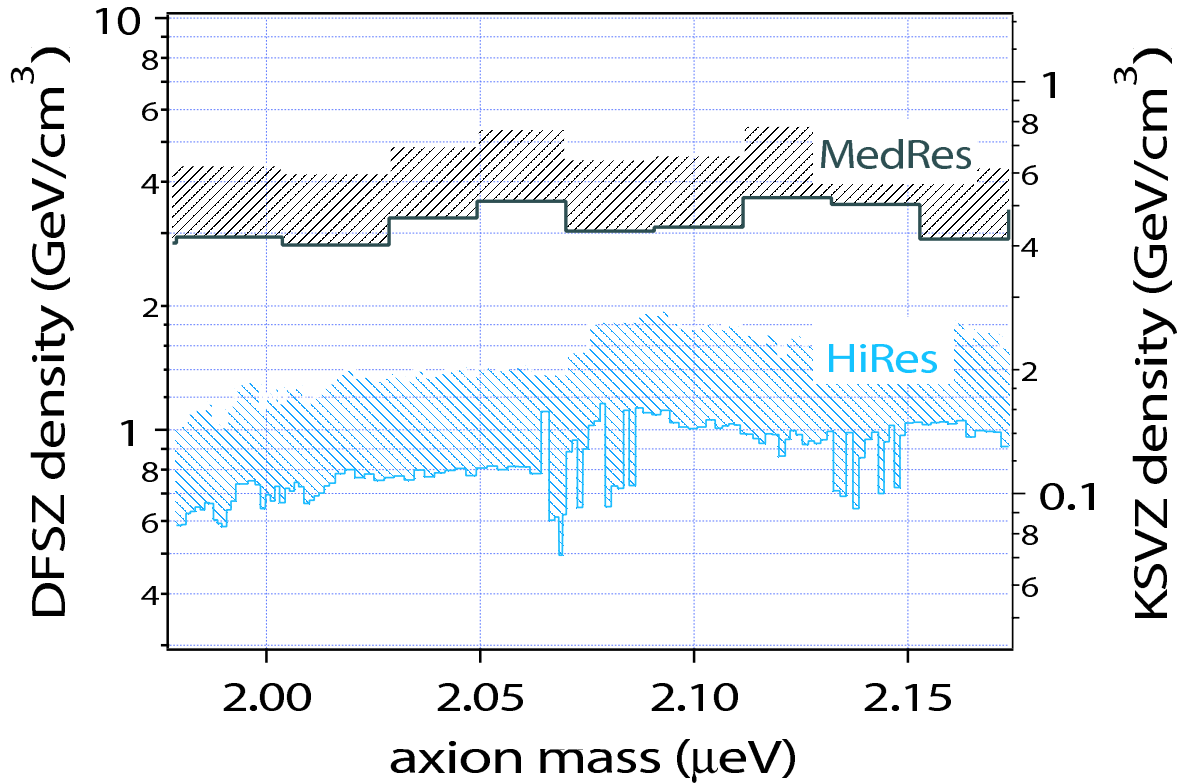


Figure 4–15. 97.7% confidence level limits for the HR 2-bin search on the density of any local axion dark matter flow as a function of axion mass, for the DFSZ and KSVZ $a\gamma\gamma$ coupling strengths. Also shown is the previous ADMX limit using the MR channel. The HR limits assume that the flow velocity dispersion is less than δv_2 given by Eq. (4–13).

4.8 Discussion

We have obtained exclusion limits on the density in local flows of cold axions over a wide range of velocity dispersions. The most stringent limit, shown in Fig. 4–15, is from the 2-bin search. For a flow velocity of 600 km/s relative to the detector, the 2-bin search corresponds to a maximum flow velocity dispersion of 10 m/s. The 1-bin search limit is less general, in that the corresponding flow velocity dispersion is half that of the 2-bin limit. It is also less stringent; much more power may be lost due to a signal occurring away from the center of a bin than in the $n = 2$ case. For $n > 2$, the limits are more general, but the larger power threshold of the searches make them less stringent.

The largest flow predicted by the caustic ring model has density 1.7×10^{-24} g/cm³ (0.95 GeV/cm³), velocity of approximately 300 km/s relative to the detector, and velocity dispersion less than 53 m/s [45]. Using Eq. (4–13) with Table 4–1 and the information displayed in Fig. 4–15 multiplied by the appropriate factors of 1.12 to obtain the 4-bin limit, it can be seen that the 4-bin search, corresponding to maximum velocity 50 m/s for $v = 300$ km/s, would detect this flow if it consisted of KSVZ axions. For DFSZ axions, this flow would be detected for approximately half the search range. These limits and the Big Flow density are illustrated in Fig. 4–16.

Figure 4–15 demonstrates that the high resolution analysis improves the detection capabilities of ADMX when a significant fraction of the local dark matter density is due to flows from the incomplete thermalization of matter that has only recently fallen onto the halo. The addition of this channel to ADMX provides an improvement of a factor of three over our previous medium resolution analysis.

It is possible that an even more sensitive limit could have been achieved with a longer integration time, as discussed in Section 4.3. This issue should be considered

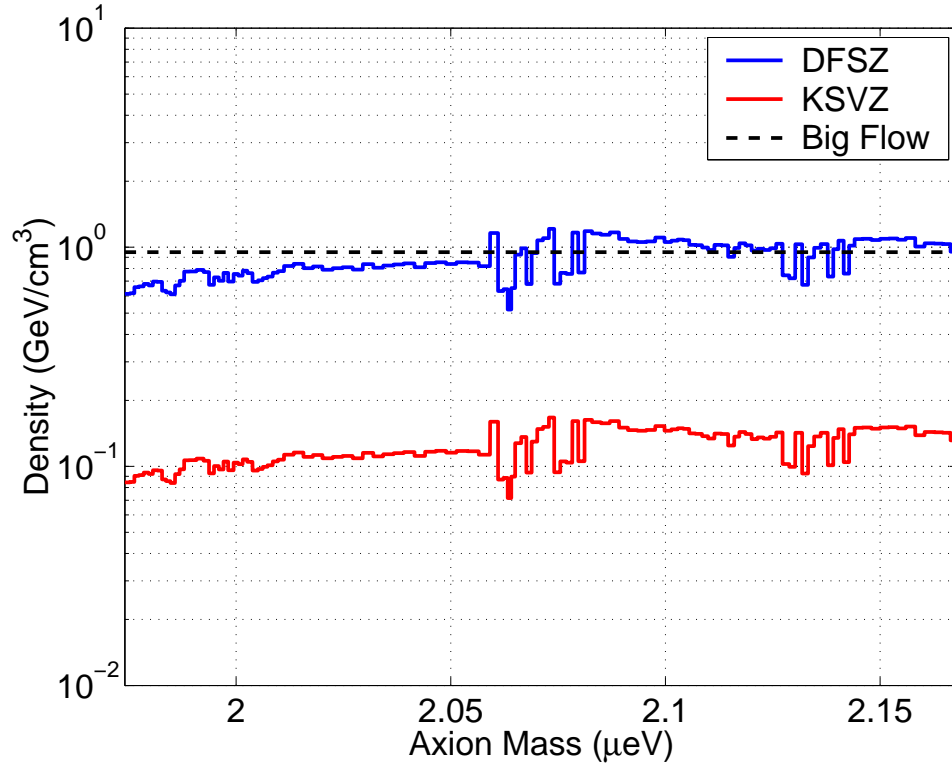


Figure 4–16. 97.7% confidence level limits for the HR 4-bin search on the density of any local axion dark matter flow as a function of axion mass, for DFSZ and KSVZ $a\gamma\gamma$ coupling strengths. Densities above the lines are excluded. For comparison, the predicted density of the Big Flow is also shown. The HR limits assume that the flow velocity dispersion is less than δv_2 given by Eq. (4–13).

at the beginning of future data runs in order to maximize the discovery potential of the HR channel.

CHAPTER 5 SUMMARY AND CONCLUSION

This work demonstrates that the new, high resolution channel of the Axion Dark Matter eXperiment improves its sensitivity for axion detection by a factor of three, provided a large fraction of the local density is in a single cold flow.

Axions present an interesting candidate for the cold dark matter component of the universe's energy density. The original motivation for the axion was to solve the strong CP problem of the standard model of particle physics. The axion is the pseudo-Nambu-Goldstone boson associated with breaking the Peccei-Quinn symmetry, implemented to solve the strong CP problem. It was later realized that the axion was also a good particle candidate for dark matter. The Peccei-Quinn symmetry breaking scale is the parameter which governs the properties of the axion and is inversely proportional to the axion mass and couplings. The axion mass is constrained to lie between 10^{-6} – 10^{-2} eV, by cosmological and astrophysical processes. Thus, the axion parameter space is bounded and we know in which range to search for the axion.

While the axion has very small couplings, it is possible to search for them by utilizing the axion-electromagnetic coupling. The Axion Dark Matter eXperiment (ADMX) uses a tunable microwave cavity detector to search for axions. When the magnetic field inside the cavity is tuned to the axion energy, resonant conversion of axions to photons will occur, which can be observed as a voltage peak in the output of the detector.

A new, high resolution channel has recently been added to the ADMX detector. This channel was designed to improve detector sensitivity by searching for axions in a specific form of halo substructure: discrete flows. The original, medium

resolution channel searches for axions in a thermalized component of the Milky Way halo. These axions have a Maxwellian velocity distribution. Axions in discrete flows have a small velocity dispersion, resulting in a narrow peak in the spectrum output by the cavity detector. The high resolution channel can search for these peaks with a high signal-to-noise ratio, improving detector sensitivity.

Discrete flows are expected to be present in the halo from tidal disruption of dwarf galaxies and from late infall of dark matter into the gravitational potential. Dark matter which has only recently fallen into the potential will not have had sufficient time to thermalize with the rest of the halo. Examining the phase-space structure of such particles shows that discrete flows will occur due to this late infall.

The first analysis for this channel has been successfully completed. After analysis of the noise background and removal of systematic effects, no axion signal was found in the mass range $1.97\text{--}2.17 \mu\text{eV}$. A broad range of flow velocity dispersions was considered by searching for signals across multiple bins by adding adjacent bins together. The new exclusion limits obtained from the high resolution channel increase the sensitivity of the ADMX detector by up to a factor of three over the previous medium resolution result. The high resolution channel thus enhances ADMX's detection ability. Should an axion signal be found, the high resolution channel will also yield valuable information about the phase-space structure of the Milky Way galactic halo.

REFERENCES

- [1] S. Perlmutter, G. Aldering, G. Goldhaber, R. A. Knop, P. Nugent, P. G. Castro, S. Deustua, S. Fabbro, A. Goobar, D. E. Groom, I. M. Hook, A. G. Kim, M. Y. Kim, J. C. Lee, N. J. Nunes, R. Pain, C. R. Pennypacker, R. Quimby, C. Lidman, R. S. Ellis, M. Irwin, R. G. McMahon, P. Ruiz-Lapuente, N. Walton, B. Schaefer, B. J. Boyle, A. V. Filippenko, T. Matheson, A. S. Fruchter, N. Panagia, H. J. M. Newberg, and W. J. Couch. Measurements of Omega and Lambda from 42 High-Redshift Supernovae. *Astrophys. J.*, 517:565–586, 1999.
- [2] A. G. Riess, A. V. Filippenko, P. Challis, A. Clocchiattia, A. Diercks, P. M. Garnavich, R. L. Gilliland, C. J. Hogan, S. Jha, R. P. Kirshner, B. Leibundgut, M. M. Phillips, D. Reiss, B. P. Schmidt, R. A. Schommer, R. C. Smith, J. Spyromilio, C. Stubbs, N. B. Suntzeff, and J. Tonry. Observational Evidence from Supernovae for an Accelerating Universe and a Cosmological Constant. *Astron. J.*, 116:1009–1038, 1998.
- [3] F. Zwicky. Spectral Displacement of Extra Galactic Nebulae. *Helv. Phys. Acta*, 6:110, 1933.
- [4] G. Bertone, D. Hooper, and J. Silk. Particle Dark Matter: Evidence, Candidates and Constraints. *Phys. Rept.*, 405:279–390, 2005.
- [5] R. D. Peccei and H. R. Quinn. CP Conservation in the Presence of Instantons. *Phys. Rev. Lett.*, 38:1440–1443, 1977.
- [6] R. D. Peccei and H. R. Quinn. Constraints Imposed by CP Conservation in the Presence of Instantons. *Phys. Rev.*, D16:1791–1797, 1977.
- [7] S. Weinberg. A New Light Boson? *Phys. Rev. Lett.*, 40:223–226, 1978.
- [8] F. Wilczek. Problem of Strong P and T Invariance in the Presence of Instantons. *Phys. Rev. Lett.*, 40:279–282, 1978.
- [9] J. E. Kim. Light Pseudoscalars, Particle Physics and Cosmology. *Phys. Rept.*, 150:1–177, 1987.
- [10] M. S. Turner. Windows on the Axion. *Phys. Rept.*, 197:67–97, 1990.
- [11] G. G. Raffelt. Astrophysical Methods to Constrain Axions and Other Novel Particle Phenomena. *Phys. Rept.*, 198:1–113, 1990.
- [12] J. E. Kim. Weak Interaction Singlet and Strong CP Invariance. *Phys. Rev. Lett.*, 43:103, 1979.

- [13] M. A. Shifman, A. I. Vainshtein, and V. I. Zakharov. Can Confinement Ensure Natural CP Invariance of Strong Interactions? *Nucl. Phys.*, B166:493, 1980.
- [14] M. Dine, W. Fischler, and M. Srednicki. A Simple Solution to the Strong CP Problem with a Harmless Axion. *Phys. Lett.*, B104:199, 1981.
- [15] A. R. Zhitnitsky. On Possible Suppression of the Axion Hadron Interactions. (in Russian). *Sov. J. Nucl. Phys.*, 31:260, 1980.
- [16] L. F. Abbott and P. Sikivie. A Cosmological Bound on the Invisible Axion. *Phys. Lett.*, B120:133–136, 1983.
- [17] J. Preskill, M. B. Wise, and F. Wilczek. Cosmology of the Invisible Axion. *Phys. Lett.*, B120:127–132, 1983.
- [18] M. Dine and W. Fischler. The Not-So-Harmless Axion. *Phys. Lett.*, B120:137–141, 1983.
- [19] R. L. Davis. Goldstone Bosons in String Models of Galaxy Formation. *Phys. Rev.*, D32:3172, 1985.
- [20] R. L. Davis. Cosmic Axions From Cosmic Strings. *Phys. Lett.*, B180:225, 1986.
- [21] D. Harari and P. Sikivie. On the Evolution of Global Strings in the Early Universe. *Phys. Lett.*, B195:361, 1987.
- [22] A. Vilenkin and T. Vachaspati. Radiation of Goldstone Bosons from Cosmic Strings. *Phys. Rev.*, D35:1138, 1987.
- [23] R. L. Davis and E. P. S. Shellard. Do Axions Need Inflation? *Nucl. Phys.*, B324:167, 1989.
- [24] A. Dabholkar and J. M. Quashnock. Pinning Down the Axion. *Nucl. Phys.*, B333:815, 1990.
- [25] R. A. Battye and E. P. S. Shellard. Global String Radiation. *Nucl. Phys.*, B423:260–304, 1994.
- [26] R. A. Battye and E. P. S. Shellard. Axion String Constraints. *Phys. Rev. Lett.*, 73:2954–2957, 1994.
- [27] M. Yamaguchi, M. Kawasaki, and J. Yokoyama. Evolution of Axionic Strings and Spectrum of Axions Radiated From Them. *Phys. Rev. Lett.*, 82:4578–4581, 1999.
- [28] C. Hagmann, S. Chang, and P. Sikivie. Axion Radiation from Strings. *Phys. Rev.*, D63:125018, 2001.
- [29] S. Chang, C. Hagmann, and P. Sikivie. Studies of the Motion and Decay of Axion Walls Bounded by Strings. *Phys. Rev.*, D59:023505, 1999.

- [30] D. H. Lyth. Estimates of the Cosmological Axion Density. *Phys. Lett.*, B275:279–283, 1992.
- [31] M. Nagasawa and M. Kawasaki. Collapse of Axionic Domain Wall and Axion Emission. *Phys. Rev.*, D50:4821–4826, 1994.
- [32] S. J. Asztalos, E. Daw, H. Peng, L. J. Rosenberg, D. B. Yu, C. Hagmann, D. Kinion, W. Stoeffl, K. van Bibber, J. LaVeigne, P. Sikivie, N. S. Sullivan, D. B. Tanner, F. Nezrick, and D. M. Moltz. Experimental Constraints on the Axion Dark Matter Halo Density. *Astrophys. J.*, 571:L27–L30, 2002.
- [33] S. Asztalos, E. Daw, H. Peng, L. J. Rosenberg, C. Hagmann, D. Kinion, W. Stoeffl, K. van Bibber, P. Sikivie, N. S. Sullivan, D. B. Tanner, F. Nezrick, M. S. Turner, D. M. Moltz, J. Powell, M.-O. Andre, J. Clarke, M. Muck, and Richard F. Bradley. Large-Scale Microwave Cavity Search for Dark-Matter Axions. *Phys. Rev.*, D64:092003, 2001.
- [34] S. J. Asztalos, R. F. Bradley, L. Duffy, C. Hagmann, D. Kinion, D. M. Moltz, L. J. Rosenberg, P. Sikivie, W. Stoeffl, N. S. Sullivan, D. B. Tanner, K. van Bibber, and D. B. Yu. An Improved RF Cavity Search for Halo Axions. *Phys. Rev.*, D69:011101, 2004.
- [35] L. Duffy, P. Sikivie, D. B. Tanner, S. Asztalos, C. Hagmann, D. Kinion, L. J. Rosenberg, K. van Bibber, D. Yu, and R. F. Bradley. Results of a Search for Cold Flows of Dark Matter Axions. *Phys. Rev. Lett.*, 95:091304, 2005.
- [36] P. Sikivie. Experimental Tests of the “Invisible” Axion. *Phys. Rev. Lett.*, 51:1415, 1983.
- [37] J. F. Navarro, C. S. Frenk, and S. D. M. White. The Structure of Cold Dark Matter Halos. *Astrophys. J.*, 462:563–575, 1996.
- [38] B. Moore, F. Governato, T. Quinn, J. Stadel, and G. Lake. Resolving the Structure of Cold Dark Matter Halos. *Astrophys. J.*, 499:L5, 1998.
- [39] P. Sikivie. Caustic Rings of Dark Matter. *Phys. Lett.*, B432:139–144, 1998.
- [40] P. Sikivie. The Caustic Ring Singularity. *Phys. Rev.*, D60:063501, 1999.
- [41] K. Freese, P. Gondolo, H. J. Newberg, and M. Lewis. The Effects of the Sagittarius Dwarf Tidal Stream on Dark Matter Detectors. *Phys. Rev. Lett.*, 92:111301, 2004.
- [42] K. Freese, P. Gondolo, and H. J. Newberg. Detectability of Weakly Interacting Massive Particles in the Sagittarius Dwarf Tidal Stream. *Phys. Rev.*, D71:043516, 2005.
- [43] P. Sikivie and J. R. Ipser. Phase Space Structure of Cold Dark Matter Halos. *Phys. Lett.*, B291:288–292, 1992.

- [44] A. Natarajan and P. Sikivie. The Inner Caustics of Cold Dark Matter Halos. *Phys. Rev.*, D73:023510, 2006.
- [45] P. Sikivie. Evidence for Ring Caustics in the Milky Way. *Phys. Lett.*, B567:1–8, 2003.
- [46] E. I. Gates, G. Gyuk, and M. S. Turner. The Local Halo Density. *Astrophys. J.*, 449:L123–L126, 1995.
- [47] S. L. Adler. Axial Vector Vertex in Spinor Electrodynamics. *Phys. Rev.*, 177:2426–2438, 1969.
- [48] J. S. Bell and R. Jackiw. A PCAC Puzzle: $\pi^0 \rightarrow \gamma\gamma$ in the Sigma Model. *Nuovo Cim.*, A60:47–61, 1969.
- [49] H.-Y. Cheng. The Strong CP Problem Revisited. *Phys. Rept.*, 158:1, 1988.
- [50] P. G. Harris, C. A. Baker, K. Green, P. Iaydijiev, S. Ivanov, D. J. R. May, J. M. Pendlebury, D. Shiers, K. F. Smith, M. van der Grinten, and P. Geltenbort. New Experimental Limit on the Electric Dipole Moment of the Neutron. *Phys. Rev. Lett.*, 82:904–907, 1999.
- [51] A. E. Nelson. Naturally Weak CP Violation. *Phys. Lett.*, B136:387, 1984.
- [52] S. M. Barr. Solving the Strong CP Problem Without the Peccei-Quinn Symmetry. *Phys. Rev. Lett.*, 53:329, 1984.
- [53] D. J. Gross, R. D. Pisarski, and L. G. Yaffe. QCD and Instantons at Finite Temperature. *Rev. Mod. Phys.*, 53:43, 1981.
- [54] P. Sikivie. Of Axions, Domain Walls and the Early Universe. *Phys. Rev. Lett.*, 48:1156, 1982.
- [55] E. W. Kolb and M. S. Turner. *The Early Universe*. Addison-Wesley Publishing Company, Reading, MA, 1994.
- [56] P. Sikivie, I. I. Tkachev, and Y. Wang. The Secondary Infall Model of Galactic Halo Formation and the Spectrum of Cold Dark Matter Particles on Earth. *Phys. Rev.*, D56:1863–1878, 1997.
- [57] P. Sikivie, I. I. Tkachev, and Y. Wang. The Velocity Peaks in the Cold Dark Matter Spectrum on Earth. *Phys. Rev. Lett.*, 75:2911–2915, 1995.
- [58] D. F. Malin and D. Carter. Giant Shells Around Normal Elliptical Galaxies. *Nature*, 285:643–645, 1980.
- [59] L. Hernquist and P. J. Quinn. Shells and Dark Matter in Elliptical Galaxies. *Ap. J.*, 312:1–16, 1987.

- [60] E. Bertschinger. Self-Similar Secondary Infall and Accretion in an Einstein-de Sitter Universe. *Astrophys. J. Suppl.*, 58:39, 1985.
- [61] J. Binney and S. Tremaine. *Galactic Dynamics*. Princeton University Press, Princeton, NJ, 1987.
- [62] S. De Panfilis, A. C. Melissinos, B. E. Moskowitz, J. T. Rogers, Y. K. Semertzidis, W. U. Wuensch, H. J. Halama, A. G. Prodell, W. B. Fowler, and F. A. Nezrick. Limits on the Abundance and Coupling of Cosmic Axions at $4.5\text{-MicroeV} < M(a) < 5.0\text{-MicroeV}$. *Phys. Rev. Lett.*, 59:839, 1987.
- [63] C. Hagmann, P. Sikivie, N. S. Sullivan, and D. B. Tanner. Results from a Search for Cosmic Axions. *Phys. Rev.*, D42:1297–1300, 1990.
- [64] C. Hagmann, D. Kinion, W. Stoeffl, K. van Bibber, E. Daw, H. Peng, L. J Rosenberg, J. LaVeigne, P. Sikivie, N. S. Sullivan, D. Tanner, F. Nezrick, M. S. Turner, D. M. Moltz, J. Powell, and N. A. Golubev. Results from a High-Sensitivity Search for Cosmic Axions. *Phys. Rev. Lett.*, 80:2043–2046, 1998.
- [65] H. Peng, S. Asztalos, E. Daw, N. A. Golubev, C. Hagmann, D. Kinion, J. LaVeigne, D. M. Moltz, F. Nezrick, J. Powell, L. J Rosenberg, P. Sikivie, W. Stoeffl, N. S. Sullivan, D. B. Tanner, M. S. Turner, and K. van Bibber. Cryogenic Cavity Detector for a Large-scale Cold Dark-matter Axion Search. *Nucl. Instrum. Meth.*, A444:569–583, 2000.
- [66] R. Bradley, J. Clarke, D. Kinion, L. J Rosenberg, K. van Bibber, S. Matsuki, M. Muck, and P. Sikivie. Microwave Cavity Searches for Dark-Matter Axions. *Rev. Mod. Phys.*, 75:777–817, 2003.
- [67] M. S. Turner. Periodic Signatures for the Detection of Cosmic Axions. *Phys. Rev.*, D42:3572–3575, 1990.
- [68] F.-S. Ling, P. Sikivie, and S. Wick. Diurnal and Annual Modulation of Cold Dark Matter Signals. *Phys. Rev.*, D70:123503, 2004.
- [69] L. D. Duffy, P. Sikivie, D. B. Tanner, S. J. Asztalos, C. Hagmann, D. Kinion, L. J Rosenberg, K. van Bibber, and D. B. Yu. A High Resolution Search for Dark-Matter Axions. *Phys. Rev.*, D74:012006, 2006.
- [70] E. J. Daw. *A Search for Halo Axions*. PhD thesis, Massachusetts Institute of Technology, Boston, MA, 1998.

BIOGRAPHICAL SKETCH

Leanne Delma Duffy was born on August 3, 1975, in Sydney, Australia. In 1980, her family moved to the Gold Coast, Australia, where she attended Miami State Primary School and Merrimac State High School. After graduating from high school, she moved to Brisbane, Australia, where she obtained a Bachelor of Science with honours in physics from The University of Queensland in 1997. She spent two years working for an environmental consulting firm, Pacific Air & Environment, Pty Ltd, and then moved to Gainesville, Florida, to study for a Doctor of Philosophy in physics.